Characterization of atypical BAR domain-containing proteins coded by *Toxoplasma gondii*

Received for publication, July 22, 2024, and in revised form, October 4, 2024 Published, Papers in Press, October 24, 2024,
https://doi.org/10.1016/j.jbc.2024.107923

Noha Al-Qatabi[1], Maud Magdeleine[1], Sophie Pagnotta[2], Amélie Leforestier[3], Jéril Degrouard[3], Ana Andreea Arteni[4], Sandra Lacas-Gervais[2], Romain Gautier[1], and Guillaume Drin[1,*]

From the [1]Université Côte d'Azur, CNRS, INSERM, Institut de Pharmacologie Moléculaire et Cellulaire, Valbonne, France; [2]Université Côte d'Azur, Centre Commun de Microscopie Appliquée, Nice, France; [3]Université Paris-Saclay, CNRS, UMR 8502, Laboratoire de Physique des Solides, Orsay, France; [4]Université Paris-Saclay, CEA, CNRS, Institute for Integrative Biology of the Cell (I2BC), Gif-sur-Yvette, France

Reviewed by members of the JBC Editorial Board. Edited by Phyllis Hanson

Toxoplasma gondii*, the causative agent of toxoplasmosis, infects cells and replicates inside *via* the secretion of factors stored in specialized organelles (rhoptries, micronemes, and dense granules) and the capture of host materials. The genesis of the secretory organelles and the processes of secretion and endocytosis depend on vesicular trafficking events whose molecular bases remain poorly known. Notably, there is no characterization of the BAR (Bin/Amphiphysin/Rvs) domain-containing proteins expressed by *T. gondii* and other apicomplexans, although such proteins are known to play critical roles in vesicular trafficking in other eukaryotes. Here, by combining structural analyses with *in vitro* assays and cellular observations, we have characterized *Tg*REMIND (regulators of membrane interacting domains), involved in the genesis of rhoptries and dense granules, and *Tg*BAR2 found at the parasite cortex. We establish that *Tg*REMIND comprises an F-BAR domain that can bind curved neutral membranes with no strict phosphoinositide requirement and exert a membrane remodeling activity. Next, we establish that *Tg*REMIND contains a new structural domain called REMIND, which negatively regulates the membrane-binding capacities of the F-BAR domain. In parallel, we report that *Tg*BAR2 contains a BAR domain with an extremely basic membrane-binding interface able to deform anionic membranes into very narrow tubules. Our data show that *T. gondii* codes for two atypical BAR domain-containing proteins with very contrasting membrane-binding properties, allowing them to function in two distinct regions of the parasite trafficking system.

Apicomplexan parasites are highly polarized cells with a secretory system that includes unique apical organelles called the micronemes and rhoptries, but also dense granules, which are more dispersed throughout the cytosol. All these organelles contain protein factors that are essential for parasite virulence. Micronemal proteins (MIC) guarantee parasite motility and host cell attachment and invasion, whereas rhoptry (ROP) and dense granule (GRA) proteins play a pivotal role in the creation and maintenance of the parasitophorous vacuole, in which the parasite develops inside a host cell, and in altering the immune response and metabolic state of the infected cell. Given the critical roles of these factors, elucidating the molecular mechanisms by which these secretory organelles are formed is of prime interest (1). For this purpose, *Toxoplasma gondii* is a powerful model for studying protein trafficking and organelle biogenesis in apicomplexan parasites.

The synthesis, sorting, and transport of MIC, ROP, and GRA proteins are tightly linked to the biogenesis of the secretory organelles (1). In *T. gondii*, the genesis of micronemes and rhoptries starts with the budding of vesicles containing ROP and MIC proproteins from the *trans* side of the Golgi apparatus. These vesicles fuse with an endosomal compartment that serves as an intermediate compartment for proteins destined for secretion and not, as in other eukaryotic cells, for recycling or degradation of endocytosed material. MIC proteins transit from the early to late regions of this endosomal-like compartment (ELC) and undergo processing by specialized proteases, mainly by the ELC-resident aspartyl protease (*Tg*ASP3) (2) but also by cathepsin L-like protease (*Tg*CPL, (3)), originating from the plant-like vacuolar compartment (4), to be transferred to the micronemes in an active form. ROP proteins are assumed to transit directly from the early endosomal compartment to prerhoptries to be processed (notably by *Tg*ASP3) into functional factors. Prerhoptries, which are large vesicles situated between the Golgi and the apical region of the parasite, undergo a process of condensation and elongation before cytokinesis, eventually developing into mature rhoptries (1). In contrast, dense granules are directly formed from the *trans*-Golgi network (TGN) in a clathrin-dependent manner following modes characteristics of both the constitutive and regulated secretory pathways observed in mammalian cells (5).

Much evidence suggests that the trafficking system of apicomplexan is divergent from those found in other eukaryotic cells like human or yeast cells, and also relies on a more limited number of components. For instance, *T. gondii* only depends on a basic set of small G-proteins Rabs (6) and lacks highly conserved endocytic factors like the components of endosomal sorting complexes required for transport or Golgi-associated, Gamma adaptin ear containing, Arf binding coat proteins

* For correspondence: Guillaume Drin, drin@ipmc.cnrs.fr.

(GGAs) that regulate the anterograde protein transport between the TGN and the endolysosomal compartments (7). Nevertheless, many standard components of the vesicle budding, transport, and fusion machineries have been identified, including N-ethylmaleimide-sensitive fusion factor (8), soluble N-ethylmaleimide-sensitive-factor attachment protein receptor (SNARE) proteins (9), subunits of the coatomer (10), clathrin adaptor complexes (11), vacuolar protein sorting proteins (12, 13), and dynamin-related protein B (14). In addition, evolutionarily conserved tyrosine and leucine-based motifs functioning in the transport and sorting of MIC and ROP protein have been characterized (15, 16). What is possibly the most fascinating is that many trafficking factors known to have given roles in well-described cellular systems are repurposed in *T. gondii* for different functions. Typically, *Tg*SORTLR, clathrin-adaptor protein 1 *Tg*AP1, and dynamin-related protein *Tg*DrpB function together at the Golgi to sort MIC and ROP protein. In contrast, their human counterparts exert their function in the endocytic/endosomal system.

Bin/Amphiphysin/Rvs (BAR) domain-containing proteins play pivotal roles in different stages of vesicular trafficking in eukaryotic cells, particularly endocytosis, but can also act as membrane remodelers (17). BAR domains form crescent-shaped homodimers that can bind and often bend membranes and, in some cases, favor membrane scission. Depending on their shape, size, and combination with membrane-binding amphipathic helices (AHs), these BAR domains are classified as BAR, N-BAR, F-BAR, or I-BAR. They impart many proteins with the capacity to sense and/or change membrane geometries. It is important to note that the behavior of these BAR domain-containing proteins intimately depends on the features of the membrane to which they bind, such as their shape but also negative charge density and tension; in some cases, the membrane-binding capacity of the BAR domain-containing proteins can be self-regulated or controlled by an external partner. Most BAR-domain-containing proteins integrate other domains or motifs, enabling them to play many functions in different subcellular regions.

At least two *T. gondii* proteins have been listed as encompassing a BAR domain (18). The first protein (TGME49_259720), predicted to have an N-terminal F-BAR domain, has been found recently to localize to internal compartments in *T. gondii*, including rhoptries, dense granules, Golgi, and post-Golgi compartments (19, 20). Remarkably, the genetic ablation of this protein, termed *Tg*REMIND (regulator of membrane-interacting domain), results in the absence of dense granules and the formation of abnormal transparent rhoptries, leading to severe inhibition of the parasite's motility, host invasion, and dissemination capabilities (20). *Tg*REMIND is also predicted to contain a C-terminal domain termed REMIND with a totally new fold and unknown function. Moreover, it has been proposed that *Tg*REMIND recognizes phosphoinositides (PIPs) *via* its F-BAR and REMIND domains to target membranes. Finally, the protein has been reported to coimmunoprecipitate with plenty of trafficking factors (20). Collectively, these data suggest that *Tg*REMIND might have an essential role in membrane trafficking and the formation of secretory organelles required for infection by *T. gondii*.

The second putative BAR domain-containing protein (TGME49_320760, called *Tg*BAR2) is localized at the cell periphery, proximal to, or sometimes colocalized with, GRA45, a marker of the inner membrane complexes (IMCs), a membrane system composed of flattened alveolar sacs that underlies the plasma membrane (PM) (19). It is still very unclear how *T. gondii* endocytoses materials. A circular invagination of the PM with a dense neck, termed the micropore, is believed to be the essential structure related to this process. Recent studies have revealed the existence of a network of proteins with homology with endocytic proteins responsible for the scaffolding of micropores but they have not identified *Tg*BAR2 as a component of this network (19, 21). Except for these few data, we have no insights into the structure and the functional traits of these two potential BAR domain-containing proteins.

To get better insights into the potential function of these two proteins, we have analyzed their structural features and membrane-binding properties *in vitro* and in a cellular context. We establish that *Tg*REMIND has an F-BAR domain that can preferentially associate with curved neutral membranes with no strict PIPs requirement. It has the intrinsic capacity to deform and potentially disrupt the membranes. Next, we show that the REMIND domain constitutes a novel kind of structural domain that tunes the ability of *Tg*REMIND to associate with the membrane *via* its F-BAR domain. These data explain the ubiquitous localization of *Tg*REMIND within the parasite and suggest it is potentially a membrane-remodeling device under the control of the REMIND domain. In parallel, we report that *Tg*BAR2 contains a BAR domain that distinguishes itself from well-known BAR domains by its extremely basic membrane-binding interface. The full-length protein targets preferentially anionic membranes, which might explain its localization at the cell periphery. It can strongly remodel the membranes and even form tubular micelles. Collectively, our data indicate that *T. gondii* codes for two atypical BAR domain-containing proteins with very contrasting features in terms of membrane targeting and remodeling power.

Results

Tg*REMIND has an F-BAR domain to bind neutral membranes with no strict PIP requirement*

The 80–348 region of *Tg*REMIND is predicted to correspond to a Fes/CIP4 homology-Bin/Amphiphysin/Rvs (F-BAR) domain (Fig. 1*A*, (20)). Figure 1*B* shows a tridimensional model of this region, established by AlphaFold (https://colab.research.google.com/github/sokrypton/ColabFold/blob/main/AlphaFold2.ipynb), which has the features of a canonical BAR: two monomers with three long α-helices arranged into a twisted coiled-coil define a six-helix bundle dimer with a crescent shape. The domain's concave face displays small patches of positive and negative charges instead of being highly basic, as found using electrostatic potential mapping (Fig. 1*C*). We expressed the 70–347 region of *Tg*REMIND appended with an N-terminal His-tag in *Escherichia coli*; this construct was then first isolated by affinity chromatography, and then

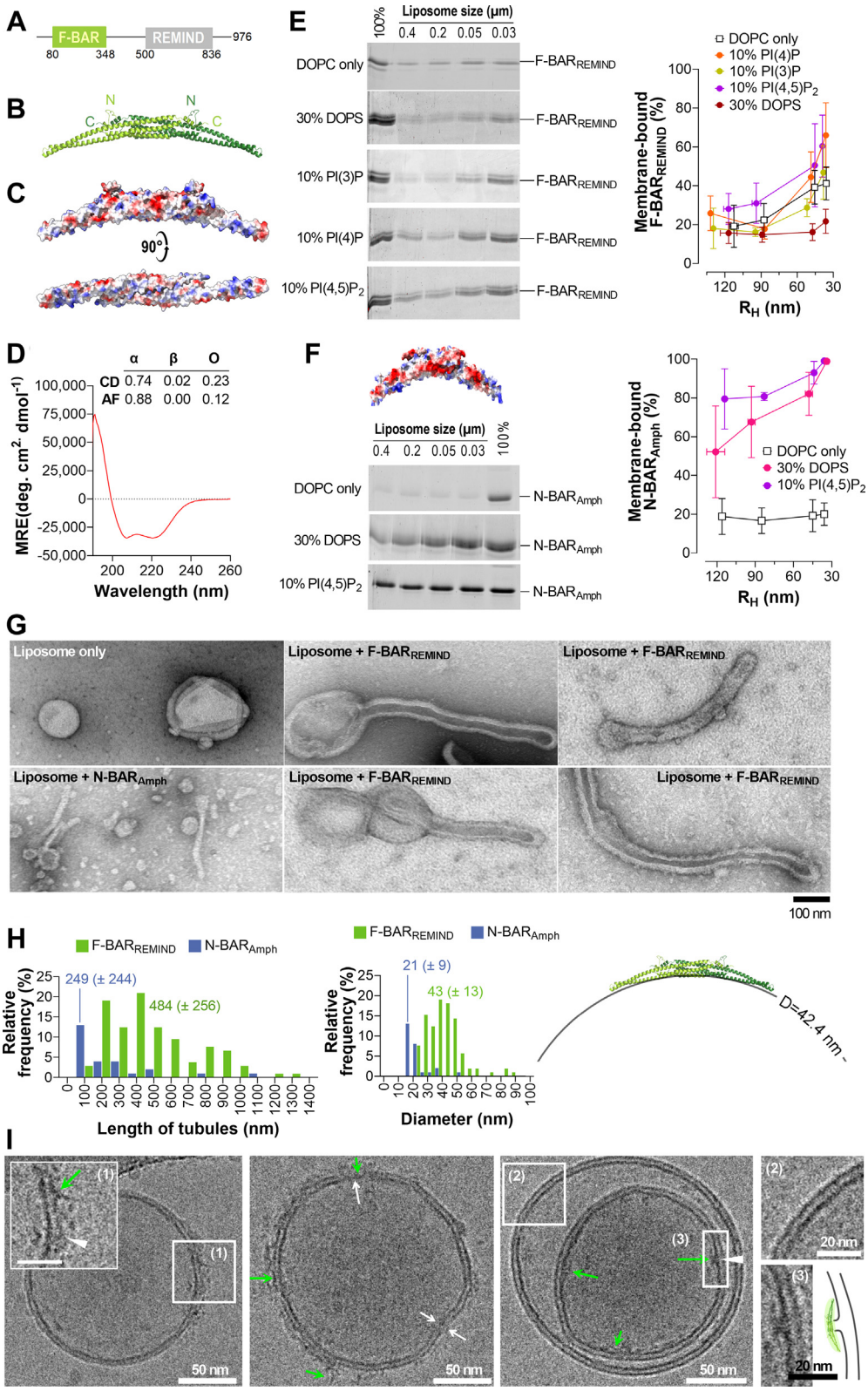

Figure 1. *Tg*REMIND F-BAR domain binds membranes with no strict PIP requirement. *A*, predicted structural organization of *Tg*REMIND. *B*, ribbon representation of the AlphaFold-predicted model of the F-BAR domain of *Tg*REMIND in a dimeric form. The position of each monomer's N- and C-terminal ends is indicated. *C*, same view as (*B*) or view of the concave face of the F-BAR domain with the surface colored by electrostatic potential (*red* = −16.9 kTe^{-1}, *blue* = +16.9 kTe^{-1}). *D*, far-UV CD spectrum of purified F-BAR_{REMIND} (3 µM) in 20 mM Tris, pH 7.4, 120 mM NaF buffer recorded at room temperature. The percentage of α-helix, β-sheet, and other structures, derived from the analyses of CD spectra (using the BeStSel method) and the AlphaFold-predicted model (using the DSSP algorithm), is given. MRE: mean residue ellipticity, H: α-helix, E: β-sheet, O: other structures. *E*, flotation assay. F-BAR_{REMIND} (0.75 µM) was incubated with liposomes (750 µM total lipids) only made of DOPC and additionally containing 30% DOPS or 10% PIPs (PI(3)P, PI(4)P or PI(4,5)P_2 at the expense of DOPC), extruded through pores of defined size, indicated at the top of the gel. This incubation was performed for 1 h at 25 °C in 50 mM Tris, pH 7.4, 150 mM NaCl (TN) buffer under constant agitation. After centrifugation, the liposomes were recovered at the top of sucrose cushions and

further purified by size exclusion chromatography (SEC). Endogenous cysteine residues, predicted to be exposed at the surface of the F-BAR domain, were substituted by alanine or serine residues to limit the aggregation of this construct during purification (Fig. S1, *A* and *B*). Gel-filtration analyses suggested that the purified protein was mainly in a trimer of dimers form or in a monomeric form (∼190 kDa or ∼38 kDa, respectively, Fig. S2, *D* and *E*). By CD spectroscopy, we established that it was folded correctly with a percentage of α-helix (74%) in excellent agreement with the percentage estimated from the AlphaFold model (Fig. 1*D*). All these data strongly suggest that the N-terminal region of *Tg*REMIND contains an F-BAR domain.

Next, we tested the capacity of this construct, referred to as F-BAR$_{REMIND}$, to bind membranes with given curvature and lipid composition using flotation assays. First, we mixed F-BAR$_{REMIND}$ with 1,2-dioleoyl-*sn*-glycero-3-phosphocholine (DOPC) liposomes of different sizes (from 130 to 35 nm in radius) obtained by sequential extrusion. Liposomes were isolated at the top of sucrose cushions after centrifugation, and membrane-bound protein was quantified using SDS-PAGE (22, 23). F-BAR$_{REMIND}$ was slightly associated (23.7% total protein) with large liposomes (with a hydrodynamic radius, $R_H \sim 120$ nm) and more with smaller ones (up to 42.4% with the smallest liposomes, $R_H < 40$ nm, Fig. 1*E*). This suggested that it could bind neutrally charged membranes in a curvature-dependent manner. Next, we tested liposomes of different sizes containing 30% of 1,2-dioleoyl-*sn*-glycero-3-phospho-L-serine (DOPS) at the expense of DOPC. We observed that F-BAR$_{REMIND}$ had a much lower avidity for these liposomes but still showed a curvature-dependent association. The fraction of membrane-bound protein increased from 15.6 to 21.7% as the liposome size decreased from 117 to 36 nm. Furthermore, we tested F-BAR$_{REMIND}$ with liposomes that contained 10% of either phosphatidylinositol 3-phosphate (PI(3)P), phosphatidylinositol 4-phosphate (PI(4)P), or phosphatidylinositol 4,5-bisphosphate (PI(4,5)P_2). We found it associated more strongly with small liposomes (36 nm) enriched with PI(4)P or PI(4,5)P_2 (up to 66% of total protein) than with small liposomes only composed of DOPC.

In parallel, we tested an archetypical BAR domain, *i.e.*, the N-BAR domain of human amphiphysin ((24, 25), residues 2–242, N-BAR$_{Amph}$) with liposomes made of DOPC only or enriched with DOPS. We observed that it bound weakly to DOPC membranes, whatever their curvature, but strongly associated with DOPS-rich membranes in a slightly curvature-dependent manner (Fig. 1*F*), in line with results obtained by Peter *et al.* (24). These results suggest that F-BAR$_{REMIND}$ does not interact with curved membranes through electrostatic interactions like N-BAR$_{Amph}$ and many other BAR domains. Instead, it can substantially bind curved, neutrally charged membranes, as observed for the F-BAR domains of the yeast proteins Rgd1p, Bzz1p, and Hof1p (Fig. S1*C*, (26)), with an avidity that can be slightly enhanced by PIPs, as also observed for Rgd1p.

F-BAR$_{REMIND}$ domain can remodel and destabilize membranes

Having determined that F-BAR$_{REMIND}$ is adapted to curved membranes, we investigated whether it could deform flat membranes as observed with other BAR-domain-containing proteins by negative-staining electron microscopy (EM) (27–31). We incubated this construct with large liposomes composed of Folch fraction I lipids (containing phosphatidylserine (PS) and PIPs) at different protein-to-lipid (P/L) molar ratios, ranging from 1/120 to 1/15. Comparatively to observations carried out with liposomes alone, we observed tubules emanating from many liposomes when incubated with F-BAR$_{REMIND}$ (Fig. 1*G*) with one, sometimes two, tubules *per* liposome (Fig. S1*D*). Tubulation was observed preferentially at high P/L ratios (1/15), suggesting that this process was dependent on the density of protein on the membrane surface (Fig. S1*E*). The length of tubules, estimated from a large set of EM pictures obtained through replicated assays with different F-BAR$_{REMIND}$ batches, was highly variable, with an average value of 484 ± 256 nm (SD). Comparatively, the diameter of tubules was very homogeneous, with an average value of 43 ± 13 nm (Fig. 1*H*). This was remarkably consistent with our estimate that the concave face of F-BAR$_{REMIND}$ would fit a membrane tubule of 42.4 nm in diameter. Comparative tests showed that N-BAR$_{Amph}$ induced the formation of narrower tubules (Fig. 1, *G* and *H*). Overall, according to our structural predictions, our results indicate that *Tg*REMIND contains a *bona fide* F-BAR domain able to induce the formation of tubules with a diameter similar to that observed for tubules induced by other F-BAR domain-containing proteins (30, 32).

To get confirmation of this phenomenon and a higher-resolution view of the membrane-binding and remodeling capacities of F-BAR$_{REMIND}$, we examined liposomes in the presence or absence of F-BAR$_{REMIND}$ (at P/L = 1/15) by cryo-EM. We observed that the F-BAR$_{REMIND}$ domain decorated

analyzed by SDS-PAGE. The amount of membrane-bound F-BAR$_{REMIND}$ was determined using the content of the first lane (100% total) as a reference based on the SYPRO Orange signal. The percentage of membrane-bound F-BAR$_{REMIND}$ is represented as the function of the average hydrodynamic radius (R_H) of liposomes. Data are expressed as mean ± SD (n = 3–5). *F*, flotation assay. N-BAR domain of human amphiphysin (N-BAR$_{Amph}$, 0.75 μM) was incubated with liposomes (750 μM lipids), only made of DOPC and additionally containing 30% DOPS or 10% PI(4,5)P_2, extruded through pores of defined size, for 1 h at 25 °C in TN buffer. The percentage of membrane-bound N-BAR$_{Amph}$ is shown as the function of the radius of liposomes (n = 3). *G*, negative-staining EM. Liposomes made of Folch fraction I lipids (30 μM lipids) and extruded through 0.4 μm pores were incubated with F-BAR$_{REMIND}$ or N-BAR$_{Amph}$ (1.9 μM) for 2 h at room temperature. A control picture of liposomes alone is shown. *H*, length and diameter distribution of membrane tubules induced by F-BAR$_{REMIND}$ (from the analysis of n = 105 tubules observed in EM images obtained in six independent experiments) or N-BAR$_{Amph}$ (n = 26, one experiment). The structure of the F-BAR domain of *Tg*REMIND seems adapted to the diameter of tubules that have been experimentally measured. *I*, Cryo-EM. Folch fraction I liposomes (90 μM lipids), extruded through 0.4 μm pores, were mixed with F-BAR$_{REMIND}$ (6 μM) at P/L = 1/15 and dialyzed three times under constant stirring in TN buffer for 30 min at cold temperature. Enlargements: (1) outer leaflet destabilization (*white arrowhead*) by F-BAR$_{REMIND}$, (2) intact bilayer, (3) outer leaflet destabilization (*white arrowhead*) by F-BAR$_{REMIND}$. *Green arrows* point to some individual F-BAR$_{REMIND}$ molecules. *White arrows* indicate local membrane disruption (*both leaflets*). The pictures are representative of two independent experiments. BAR, Bin/Amphiphysin/Rvs; PIPs, phosphoinositides; DOPC, 1,2-dioleoyl-*sn*-glycero-3-phosphocholine; DOPS, 1,2-dioleoyl-*sn*-glycero-3-phospho-L-serine; P/L, protein-to-lipid; REMIND, regulator of membrane-interacting domain.

the surface of liposomes and modified the bilayer (Fig. 1*I*, green arrows); however, no tubules were seen in our experimental conditions. Interestingly, we observed that the F-BAR$_{REMIND}$ interacted with the outer or inner leaflet of the membrane and, in some areas, disrupted either or both leaflets (Fig. 1*I*, white arrowheads, and arrows, respectively). Moreover, we also observed some proteins within the interior of the liposomes, confirming that the integrity of the membrane was lost (Fig. 1*I*, white arrow). Collectively, these data show the capacity of the F-BAR$_{REMIND}$ to interact with membranes, locally modify their shape, and potentially disrupt them.

Impact of charge reversal mutations on the membrane-binding properties of F-BAR$_{REMIND}$

We mentioned above the resemblance between F-BAR$_{REMIND}$ and the F-BAR domain of Rgd1p regarding membrane-binding capacities. Interestingly, the Rgd1p F-BAR domain can make specific contacts with the polar head of PIPs *via* a cluster of basic residues localized in its concave face (26). We identified an analogous, albeit smaller, cluster in F-BAR$_{REMIND}$ composed of the K210, R214, R217, and R250 residues (Figs. 2*A*). Therefore, we designed three mutants in which two out of these four residues were substituted by anionic residues (R214E/R217E, R217E/R250E, K210D/R214E). This markedly impacts the electrostatic features of the concave face of the F-BAR domain (Fig. 2*B*). We purified the corresponding mutants (Fig. S2, *A* and *B*) and assessed that they were adequately folded by CD spectroscopy (Fig. S2*C*). Using flotation assays, we found that, overall, these mutated forms of F-BAR$_{REMIND}$ bound only slightly less to PI(4,5)P_2-containing liposomes compared to the WT form, notably when these liposomes were large (Fig. 2*C*). The most defective mutant was the R214E/R217E mutant, suggesting that R214 and R217 residues could be primarily involved in recognizing PIPs. Because F-BAR$_{REMIND}$ substantially binds to neutral membranes, we also examined the potential role of hydrophobic interaction in the membrane-binding process. We identified a portion of the lateral side of F-BAR as highly hydrophobic and substituted two hydrophobic residues with anionic ones to obtain an L201D/M212E mutant (Fig. S2*F*). Albeit well-folded (Fig. S2, *A*–*E*), this construct was impaired in its capacity to bind liposomes, whatever their size, comparatively to the WT form of F-BAR$_{REMIND}$ (Fig. 2*D*). However, EM observation showed that all these mutants deformed liposomes in tubulation assays at a high P/L ratio (Fig. 2*E*). We conclude that the interaction of F-BAR$_{REMIND}$ with the membrane is not primarily dictated by specific interaction with PIPs but most probably by a combination of hydrophobic and short-range electrostatic interaction.

REMIND domain is a new structural domain without any membrane-binding capacity

The 500–840 region of the *Tg*REMIND protein is predicted by AlphaFold to be composed of fifteen α-helices and three β-sheets (Fig. 3*A*). This domain, referred to as REMIND, has no homology with any other known structural domains (20). We examined whether this predicted structure remained stable in water during a 1-μs long molecular dynamics (MD) simulation. As shown in Figure 3*B*, we observed no structure unfolding over time, with a RMSD inferior to 0.7 nm. By calculating the root-mean-square fluctuation (RMSF) for each Cα of the protein backbone (Fig. 3*C*), we identified that the N- and C-terminal ends of the protein were mobile, as were three intrinsically disordered linkers between α1 and α2 helices, α2 and α3 helices, and α8 helix and β3 sheet. We also noted that a couple of α-helices (α10 and α11) were mobile yet without getting unfolded. Collectively, these data suggest that the region 500–840 of *Tg*REMIND corresponds to a stable structural domain.

To further demonstrate this, we purified the [495–840] region of *Tg*REMIND comprising the REMIND domain to experimentally determine its structure (Fig. S3). Unfortunately, attempts to crystallize this protein were unsuccessful. We therefore performed CD measurements to determine whether this construct was folded and, if true, to estimate its secondary structure content. We obtained a spectrum with two minima at 206–208 nm and 222 nm, indicating that the construct was well-folded (Fig. 3*D*). Then, we compared this spectrum with spectra generated from a series of 50 conformations adopted by the predicted REMIND domain during the one μs-MD simulation and found an excellent match. The CD spectrum analysis indicated that the construct is mainly helical (up to 60% helix) with a low β-sheet content in agreement with the corresponding values inferred from the tridimensional model. Additionally, we measured the intrinsic fluorescence of the REMIND domain by recording the emission fluorescence spectrum of tryptophan residues (eight in the purified construct). A maximum fluorescence intensity was measured at λ = 338 nm (Fig. 3*E*). In comparison, we obtained a maximum fluorescence intensity at λ = 352 nm with free L-tryptophan in solution. These data indicated that some tryptophan residues of REMIND are buried in a hydrophobic environment, as predicted by the AlphaFold model. Jointly, our data establish the REMIND domain as being a new kind of structural domain whose folding probably corresponds to that predicted *in silico*.

Next, we tested whether the REMIND domain could bind to membranes. This construct (0.75 μM) was mixed with liposomes (750 μM lipids) of various sizes, either only composed of DOPC or doped with 10% PI(4,5)P_2. We found that REMIND did not bind to these liposomes, whatever their composition and curvature, in stark contrast to F-BAR$_{REMIND}$, used as a positive control (Fig. 3*F*); moreover, we observed that REMIND, even at high P/L (1/30), could not deform liposomes (Fig. 3*G*). At odds with previous results based on protein-lipid overlay assays (20), our data suggest that the REMIND domain has no ability to bind membranes and instead has another function.

F-BAR$_{REMIND}$ but not REMIND domain can bind endomembranes

To strengthen our conclusions based on *in vitro* assays while also getting more insights into the features of F-BAR$_{REMIND}$

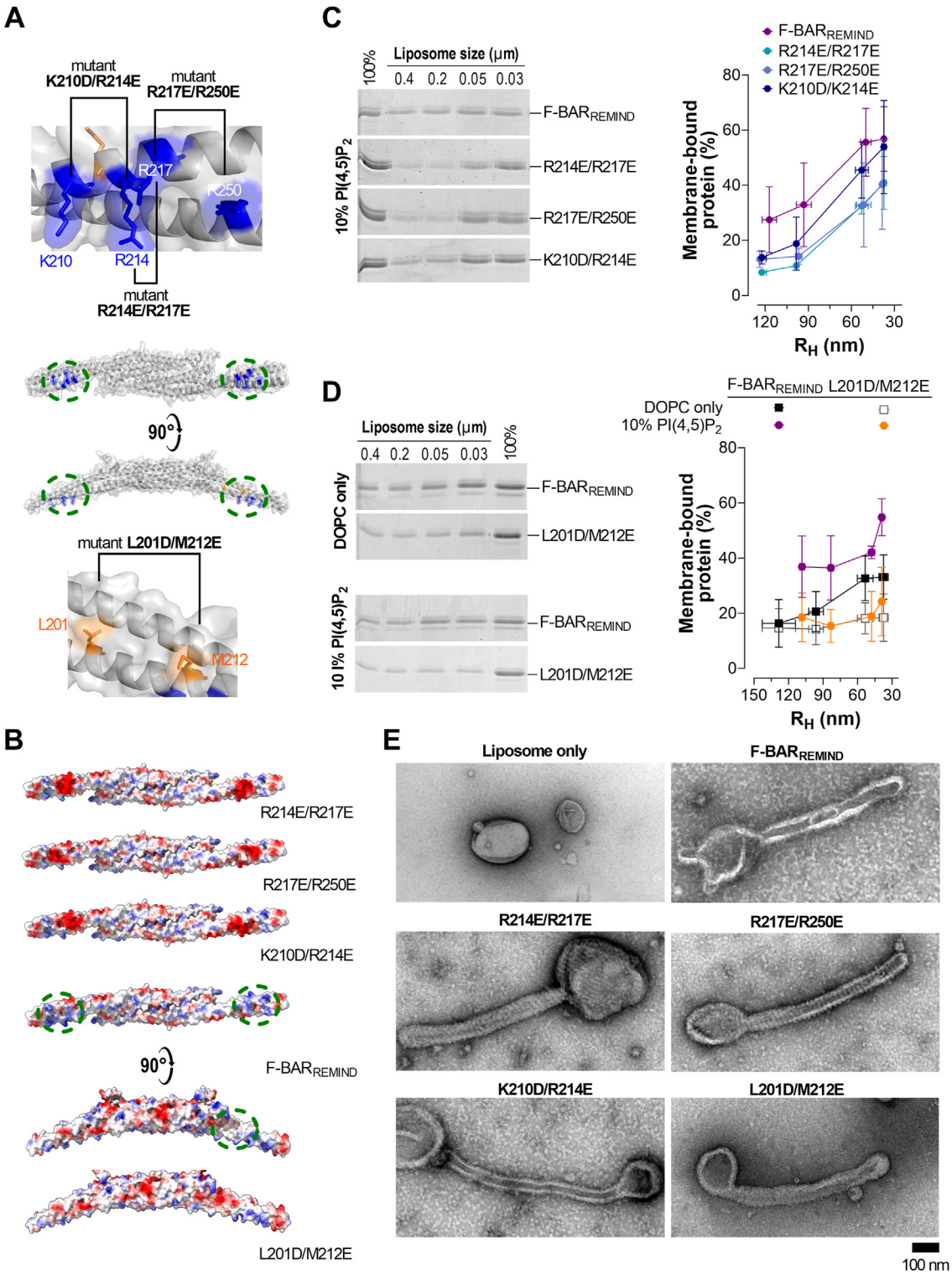

Figure 2. Charge reversion in the concave face and lateral side of F-BAR$_{REMIND}$ affects how it binds to and deforms membranes. *A*, localization of arginine and lysine residues that constitute a basic cluster in the concave face of F-BAR$_{REMIND}$ (in *blue*) and localization of solvent-exposed hydrophobic residues in the lateral side of this domain (in *orange*). These residues were substituted by anionic residues (aspartate or glutamate) to test their contribution to the F-BAR$_{REMIND}$/membrane interaction. *B*, electrostatic features of the molecular surface of F-BAR$_{REMIND}$ and its mutated forms (*red* = −16.9 kTe^{-1}, *blue* = +16.9 kTe^{-1}). *C*, flotation assay. F-BAR$_{REMIND}$ or K210D/R214E, R214E/R217E or R217E/R250E mutant (0.75 µM) was incubated with liposomes composed of DOPC/PI(4,5)P$_2$ (90:10, 750 µM lipids), with a defined radius, for 1 h at 25 °C. Data are represented as mean ± SD (n = 3–5). *D*, flotation assay. F-BAR$_{REMIND}$ or L201D/M212E mutant (0.75 µM) was incubated with liposomes (750 µM) composed of DOPC or DOPC/PI(4,5)P$_2$ (90:10), with a defined radius, for 1 h at 25 °C. Mean ± SD (n = 3–4). *E*, negative-staining EM. Liposomes made of Folch fraction I lipids (30 µM) were incubated with F-BAR$_{REMIND}$ or its mutated forms (1.9 µM) for 2 h at room temperature. A control picture of liposomes only is shown. BAR, Bin/Amphiphysin/Rvs; DOPC, 1,2-dioleoyl-*sn*-glycero-3-phosphocholine; REMIND, regulator of membrane-interacting domain.

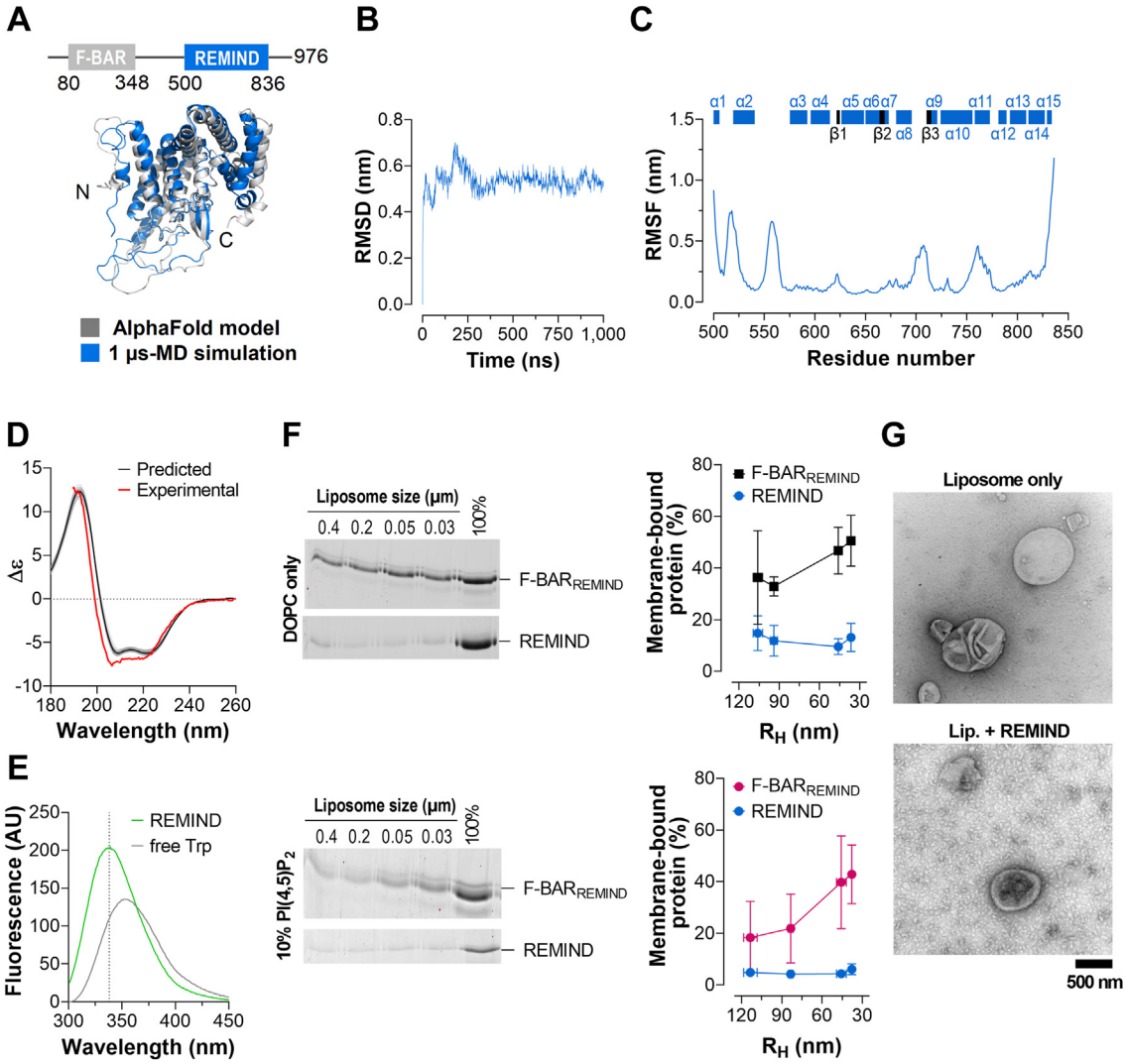

Figure 3. REMIND region encompasses a folded domain with no membrane-binding capacity. *A*, ribbon representation of the three-dimensional model of the REMIND domain (region 500–836 of *Tg*REMIND) established by AlphaFold (in *gray*) and of the final conformation of this domain after 1 µs-MD simulation in water (in *blue*). The N- and C-terminal ends of the domain are indicated. *B*, RMSD of the Cα atoms with respect to the starting and equilibrated structure of the REMIND domain as a function of time. *C*, the RMSF value of atomic positions of each Cα atom of the REMIND domain, indicative of the internal motions of this domain, is shown. The localization of α-helix and β-sheet along the sequence is indicated. *D*, predicted and experimental CD spectra of the REMIND domain. Spectra were predicted from configurations of the REMIND domain collected every 10 ns during the MD simulation (*gray spectra*) using the PDBMD2CD algorithm. An average spectrum is represented in *black*. For comparison, the far-UV CD spectrum of purified *Tg*REMIND [495–840] construct (REMIND, 2 µM) in 20 mM Tris, pH 7.4, 120 mM NaF buffer at room temperature is shown (in *red*). *E*, the intrinsic fluorescence of REMIND (1 µM) was measured in TN buffer at 30 °C. A spectrum was measured with free L-tryptophan (4 µM) as a comparison. *F*, flotation assay. REMIND (0.75 µM) was incubated with liposomes (750 µM lipids) of different mean radii, composed of DOPC or DOPC/PI(4,5)P_2 (90:10) for 1 h at 25 °C under agitation. Data are represented as mean ± SD (n = 3–4). *G*, negative-staining EM images of liposomes (30 µM lipids), composed of Folch fraction I lipids, mixed or not with REMIND (1.9 µM). DOPC, 1,2-dioleoyl-*sn*-glycero-3-phosphocholine; MD, molecular dynamics; RMSF, root mean square fluctuation; REMIND, regulator of membrane-interacting domain.

and REMIND domains, we analyzed whether overexpressing these domains separately or the full-length *Tg*REMIND induced membrane remodeling in a cellular context. Such a strategy was used to define the functional traits of diverse BAR domain-containing proteins (24, 33–35) better. Because the transgenic expression of the F-BAR domain of *Tg*REMIND is toxic for *T. gondii* (20), it was interesting to compare our constructs in a human retinal pigment epithelial-1 (RPE-1) cell line used as a surrogate system. We expressed the full-length *Tg*REMIND protein tagged with an N-terminal GFP (GFP-*Tg*REMIND) for 24 h in the cells and made two observations by fluorescence microscopy: the protein was mostly cytosolic, and the Golgi apparatus, whose *cis*- and *trans*-cisternae were labeled with GM130 and TGN46, respectively, was disorganized and compacted (Fig. 4*A*). In cells where the GFP-tagged form of the F-BAR_{REMIND} domain was expressed, we observed even more drastic changes in the Golgi morphology along with the apparition of green puncta dispersed throughout the cytoplasm. In contrast, GFP-REMIND was fully cytosolic, and the Golgi structure was unaltered. Jointly, these results confirm that the BAR but not the REMIND domain confer to *Tg*REMIND the capacity to perturb cell membranes.

To better understand the properties of F-BAR_{REMIND}, we analyzed its cellular localization and the structure of the Golgi

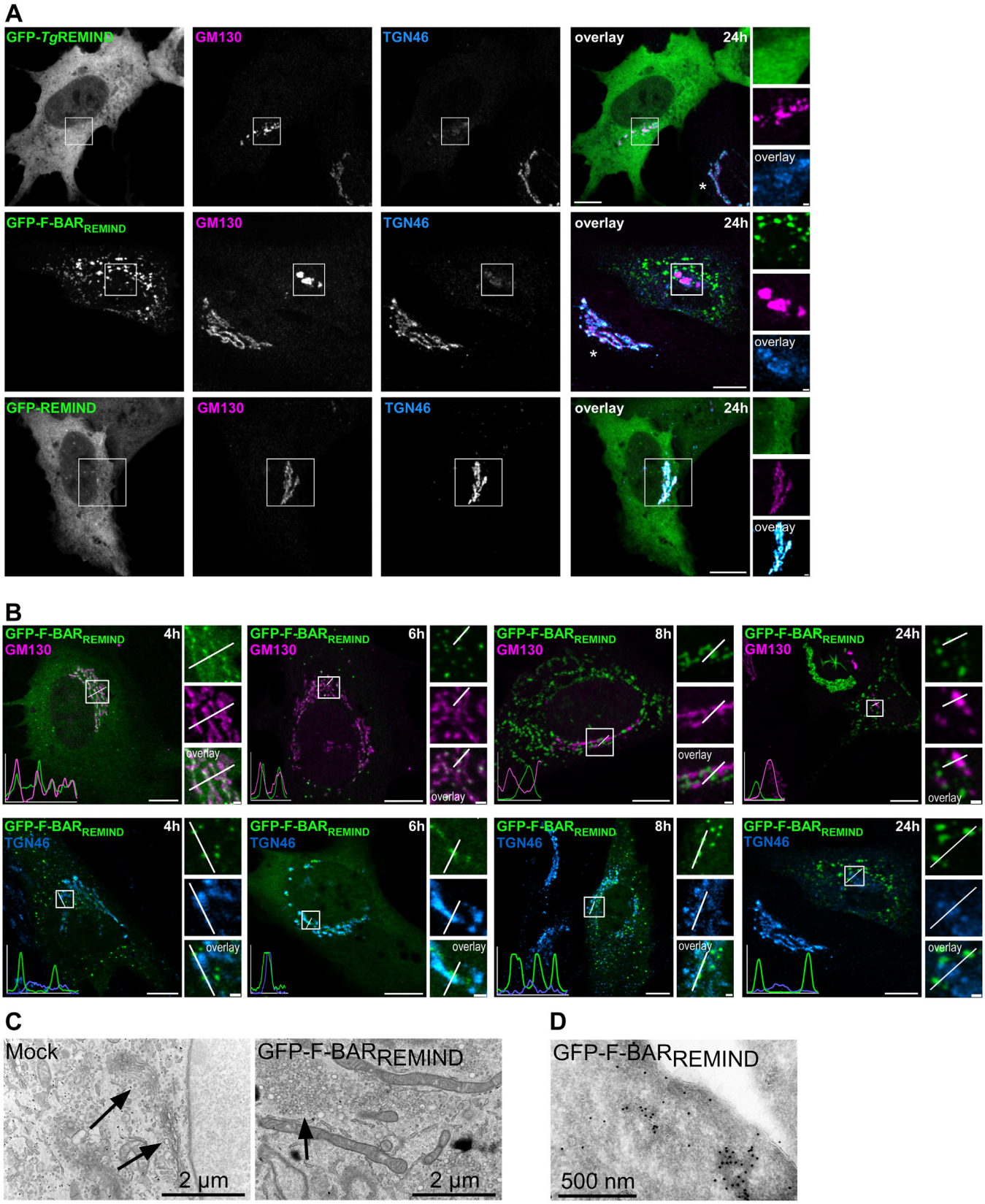

Figure 4. F-BAR$_{REMIND}$ binds to the surface of the Golgi apparatus and causes its disruption. *A*, localization of GFP-F-BAR$_{REMIND}$, GFP-*Tg*REMIND, or GFP-REMIND constructs expressed for 24 h in RPE-1 cells. Before observations by confocal microscopy (Leica TCS SP8, 63 × , NA 1.4), cells were fixed and then labeled with an anti-GM130 antibody (*magenta*) and anti-TGN46 antibody (*blue*). *Stars* indicate the presence of a standard Golgi apparatus in non-transfected cells. The images are representative of the localization of GFP-F-BAR$_{REMIND}$, GFP-*Tg*REMIND, or GFP-REMIND observed in many cells in which these constructs were expressed (number of cells, GFP-F-BAR$_{REMIND}$, n = 48 from five independent experiments; GFP-*Tg*REMIND, n = 49, four independent experiments; GFP-REMIND, n = 15, three independent experiments).*B*, representative picture of the localization of GFP-F-BAR$_{REMIND}$ in RPE-1 cells at different

apparatus at different time points after transfection of RPE-1 cells (4, 6, 8, and 24 h). We observed that the ribbon-like structure of the Golgi apparatus was maintained at short times (≤ 6 h) and that the GFP-F-BAR$_{REMIND}$ signal was colocalized or juxtaposed to that of GM130 and TGN46, which suggested that the BAR domain was bound to the Golgi membrane (Fig. 4*B*). We confirmed that, after a longer post-transfection time, the Golgi apparatus underwent intense disorganization and that many dispersed green dots appeared in the cytoplasm. To better understand this phenotype, we analyzed the ultrastructure of cells in which GFP-F-BAR$_{REMIND}$ was expressed for 24 h, by transmission EM. Compared to cells transfected with an empty plasmid (mock), we observed clusters of small vesicles in place of the typical Golgi structure, indicative of its fragmentation, in line with our observations by light microscopy (Fig. 4*C*). Additionally, using immunogold labeling we identified aggregates that could be strongly labeled with an anti-GFP antibody, indicating that they were composed of GFP-F-BAR$_{REMIND}$ (Fig. 4*D*). Because the expression of GFP-F-BAR$_{REMIND}$ did not perturb the cytoskeleton organization, we concluded that this construct likely altered the Golgi structure by directly interacting with its surface (Fig. S4*A*). In cells expressing *Tg*REMIND, we observed a gradual disorganization of the Golgi apparatus over time but not a clear colocalization or proximity between this construct and Golgi markers (Fig. S4*B*). As expected, no change in the Golgi structure was seen with GFP-REMIND (Fig. S4*B*). These results support the idea that the BAR domain but not the REMIND can associate with membranes, leading to their morphological change, corroborating our *in vitro* data. Interestingly, *Tg*REMIND localized weakly with Golgi markers compared to its BAR domain alone, suggesting that the REMIND domain can somehow modulate the association of the F-BAR$_{REMIND}$ domain with membranes.

REMIND domain prevents Tg*REMIND from interacting with membranes* via *its F-BAR domain*

To further define the potential role of the REMIND domain, we first examined how purified full-length *Tg*REMIND (Fig. S5, *A* and *B*) bound to membranes compared to F-BAR$_{REMIND}$. Using flotation assays, we found that it was weakly associated with PI(4,5)P_2-containing liposomes, even those of the smallest size (≤ 30% of total protein), comparatively to F-BAR$_{REMIND}$ (Fig. 5*A*, also compare to data shown in Figs. 1 and 2). This supported the idea that the REMIND domain could regulate the membrane-binding capacity of the F-BAR$_{REMIND}$ domain. To explore this, we performed flotation assays in which F-BAR$_{REMIND}$ was incubated with liposomes in the absence or presence of a stoichiometric amount of REMIND. Remarkably, we found that the percentage fraction of F-BAR$_{REMIND}$ bound to small liposomes composed of DOPC dropped from ∼44 to 8% if it was premixed with REMIND (Fig. 5*B*). Similar results were obtained with liposomes doped with 10% PI(4,5)P_2. To confirm these results, we evaluated whether F-BAR$_{REMIND}$ could tubulate liposomes in the presence of the REMIND domain by negative staining EM. Contrary to the control experiment performed with the F-BAR domain alone, we observed no tubulation despite an extensive inspection (Fig. 5*C*). Collectively, these data strongly suggest that the REMIND domain can prevent the F-BAR$_{REMIND}$ domain from binding membranes.

Remarkably in line with our data, the analysis of structural models of the *Tg*REMIND protein (encompassing residues 72–838 of the full-length protein) predicted that the REMIND domain is associated with the tip of the F-BAR$_{REMIND}$ domain (Fig. 5, *D* and *E*, and (20)). We ran three independent 250 ns-long MD simulations of the protein in solution to further analyze this potential intramolecular interaction. We observed a high increase in the RMSD values (Fig. S5C), which mainly corresponds to significant movements of the linker region between the BAR and REMIND domains and some fluctuations inside the REMIND domain, as indicated by visualizing the MD trajectories (see Movie S1) but also by calculating the RMSF for each residue (Fig. S5*D*). Along with this, we observed that the extremity of the BAR domain (region 214–259) remained in close association with the REMIND domain along each trajectory, as indicated by the average distances and associated standard-deviation values calculated for pairs of residues, one belonging to the F-BAR domain, the other to the REMIND domain (Figs. 5*F* and S6). Interestingly, a search for evolutionary conservation in *Tg*REMIND sequences revealed that the region of REMIND in interaction with the F-BAR domain includes many highly conserved residues (Figs. 5, *E* and *F*, S5*E*, and S7). Analysis of MD trajectories showed that some of these (K530, K609, E736, S743, E744, Q747, E753, R773, N774, and E811, conservation score ≥ 7) can form one or more H-bonds with residues belonging to the F-BAR domain, some of these being also well-conserved (Y215, S219, Q230, P237, R240, T241, and A244, Figs. 5, *E* and *G* and S7). These data support the notion that the REMIND domain can stably interact with the BAR domain to prevent its interaction with membranes.

Tg*BAR2 strongly binds and deforms anionic membranes*

A second protein in *T. gondii* of unknown function (GenID TGME49_320760) composed of 357 amino-acids was predicted by AlphaFold to contain a BAR domain (region 14–213) followed by a disordered region (Figs. 6*A* and S8*A*). A close analysis of the structural model suggested that the BAR domain may be adapted to highly curved membranes, able to

time points (4, 6, 8, or 24 h) after transfection (for each time point, n = 8–11 cells from two independent experiments). Cells were fixed and labeled with antibodies against GM130 or TGN46. The overlay panel shows *merged* channels. *Line scan* shows fluorescence intensities of the *green*, *magenta*, or *blue* channels along the *white arrows* shown in the insets. The scale bar represents 10 μm (inset, 1 μm). *C*, EM images of RPE-1 cells transfected for 24 h with empty vector (mock) or vector expressing GFP-F-BAR$_{REMIND}$. The *arrow* points to a standard Golgi apparatus (*left picture*) or vesicle clusters (*right image*). The scale bar represents 2 μm. *D*, immunogold labeling. GFP-F-BAR$_{REMIND}$ (beads: 5 nm) are enriched in aggregates localized in the cytosol. The scale bar represents 500 nm. These EM images are representative of three independent experiments. BAR, Bin/Amphiphysin/Rvs; RPE-1, retinal pigment epithelial-1; REMIND, regulator of membrane-interacting domain; TGN, *trans*-Golgi network.

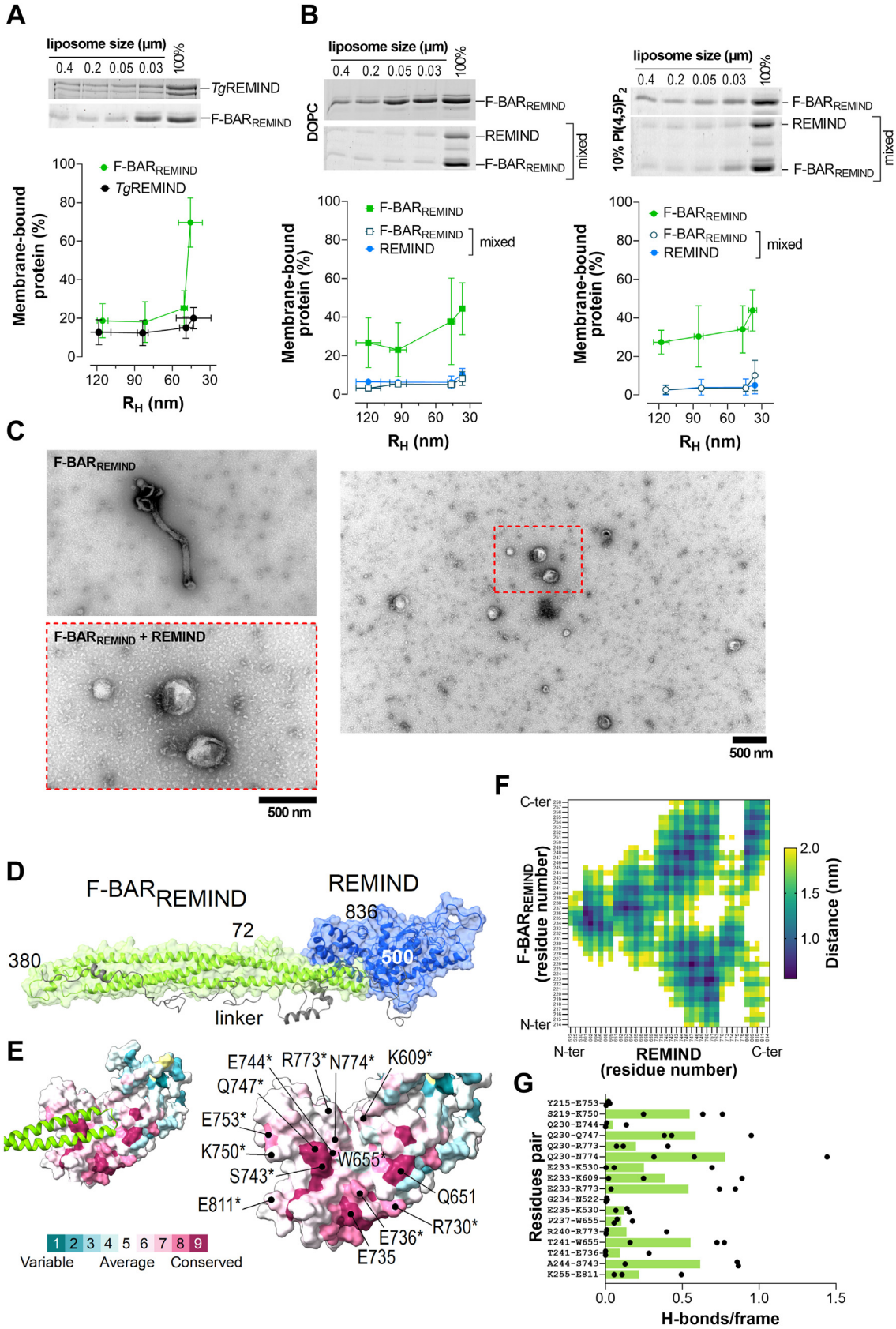

Figure 5. REMIND-dependent inhibition of the membrane-binding capacity of *Tg*REMIND. *A*, flotation assays. *Tg*REMIND (0.75 µM) was incubated with liposomes (750 µM lipids) of different sizes, composed of DOPC/PI(4,5)P_2 (90:10) for 1 h at 25 °C under agitation. Data are represented as mean ± SD (n = 3). *B*, F-BAR$_{REMIND}$ was mixed alone or together with a stoichiometric amount of REMIND with liposomes of different sizes, composed of DOPC only or DOPC/PI(4,5)P_2 (90:10) for 1 h at 25 °C under agitation. Mean ± SD (n = 3–5). *C*, negative staining EM. Representative images of Folch fraction I liposomes incubated with F-BAR$_{REMIND}$ alone or mixed with REMIND. A large view shows that no tubule emanates from liposomes when the REMIND domain is present. *D*, a

fit a membrane tubule of ∼22 nm in diameter. Moreover, we estimated that its concave face is extremely positively charged compared to that of F-BAR$_{REMIND}$ (Fig. 6*B*) but also even more basic than that of archetypical BAR and N-BAR domains belonging to amphiphysin, endophilin, and arfaptin (Fig. S8*B*). To define the membrane-binding properties of this protein (hereafter called *Tg*BAR2), we expressed its recombinant form in *E. coli* and purified it by affinity chromatography and SEC. However, the purity of the preparation was not high enough to accurately assess the folding of the protein by CD spectroscopy. Therefore, using flotation assays, we directly analyzed its ability to associate with liposomes of given compositions and sizes. We found that the protein was hardly associated with DOPC liposomes, whatever their size, but, in contrast, was firmly bound to membrane enriched with either 10% PI(4,5)P_2 or 30% DOPS in a somewhat curvature-dependent manner (Fig. 6*C*). Next, we directly compared the membrane-binding properties of *Tg*BAR2 with those of F-BAR$_{REMIND}$ in the same flotation assays. We confirmed that F-BAR$_{REMIND}$ but not *Tg*BAR2 was associated with pure PC membranes. An opposite result was obtained with membranes enriched in PS and additionally in PI(4,5)P_2 (Fig. 6*D*). Next, we investigated whether *Tg*BAR2 could remodel liposomes composed of Folch fraction I lipids at P/L = 1/15 by negative-staining EM. Remarkably, for each condition, we found that *Tg*BAR2 caused the massive formation of narrow and wider tubules with a mean diameter of 16 ± 4 and 34 ± 6 nm, respectively (Fig. 6, *E* and *F*), *i.e.*, narrower than those generated by F-BAR$_{REMIND}$. Moreover, these tubules were, on average, longer than those generated by F-BAR$_{REMIND}$ (1117 ± 933 nm as measured for the ticker tubules, Fig. 6*F*). It is also noteworthy that *Tg*BAR2 generated more tubules *per* liposome than F-BAR$_{REMIND}$ (Fig. S8*C*). To get a higher-resolution view of the membrane-remodeling capacity of *Tg*BAR2, we examined how the protein deformed liposomes by cryo-EM. We confirmed its ability to induce the formation of narrow and broader tubules (Fig. 6, *G* and *H*). We observed that the protein forms tubular micelles (Fig. 6*G*, black arrow) with a width of ∼ 10 nm (Fig. 6*H*), deriving only from the outer leaflet of the liposomes or deforms liposomes into tubules with a width of ∼ 24 nm, delimited by a lipid bilayer (Fig. 6*G*, white arrow; Fig 6*H*). *Tg*BAR2 coated the membrane surfaces and interacted with the leaflets. Transmembrane densities were also visible (Fig. 6*G*, yellow arrows). By analyzing the sequence of *Tg*BAR2, we did not identify any membrane-binding AHs or hydrophobic wedges that might account for the remodeling capacity of this protein (Fig. S8*D*). Collectively, these data suggest that the structural and electrostatic features of the BAR domain of *Tg*BAR2 give this protein a much higher propensity to bind and deform negatively charged membranes compared to F-BAR$_{REMIND}$.

Discussion

The formation of specific secretory compartments in apicomplexans, containing many of the factors the parasite uses to invade and reside in its host, relies on specialized vesicular trafficking pathways, the features of which remain poorly described. In this context, the role of BAR domain-containing proteins is barely known. This study reports the first biochemical characterization of *Tg*REMIND and *Tg*BAR2, two BAR domain-containing proteins expressed in *T. gondii*, a model parasite of the phylum Apicomplexa.

First, we demonstrate that the N-terminal region of *Tg*REMIND contains an F-BAR domain (F-BAR$_{REMIND}$). We show that this region is well-folded, has a CD signature that matches the structural predictions, and has a dimerization capacity. Furthermore, we establish that this domain associates with liposomes less than 60 nm in radius better than with liposomes of higher radius, indicating that it is adapted to positively curved membranes, as observed for some BAR domains [*e.g.*, in centaurin (24)) and F-BAR domains [*e.g.*, in Syndapin 1) (36)]. Most notably, using a gold-standard procedure based on the observation of liposomes by negative-staining EM (24, 32), we find that F-BAR$_{REMIND}$ can generate ∼ 40 nm diameter tubules. Remarkably, as estimated from our structural model, the intrinsic curvature of F-BAR$_{REMIND}$ is perfectly compatible with generating such tubules. Knowing that F-BAR domain-containing proteins can form tubules with diameter >25 to 30 nm [*e.g.*, F-BAR domain of FCho2 (32, 33), Syndapin/Pacsin (28, 33, 37), and CIP4 (30, 33)] whereas proteins with BAR and N-BAR domains predominantly generate narrower tubules ≤ 30 nm [N-BAR domain of amphiphysin and endophilin-A, BAR domain of arfaptin (24, 38, 39)], our data demonstrates that *Tg*REMIND contains a *bona fide* F-BAR domain. It is worth noting that many F-BAR domain-containing proteins deform liposomes into a wide range of tubule diameters due to their capacity to adopt diverse orientations relative to the tubule axis (30, 32, 40). In our assays, F-BAR$_{REMIND}$ generates tubules that are relatively homogenous in diameter, suggesting that this domain adopts one major single orientation at the membrane surface.

F-BAR$_{REMIND}$ can substantially bind to pure PC membranes, and this association is only slightly enhanced by PIPs, whereas an abundance of PS inhibits it. This indicates that *Tg*REMIND has membrane-binding specificities that differ

three-dimensional model of the full-length *Tg*REMIND established by AlphaFold shows the association between the REMIND domain and the tip of the F-BAR domain. Only one monomer is shown. *E*, close-up view of F-BAR binding site predicted at the surface of the REMIND domain showing the degree of amino acid conservation based on 37 distinct sequences from diverse apicomplexan species. Residues that are highly conserved and/or able to form one or more hydrogen bonds with residues of the BAR domain are indicated (a *star* indicates whether a residue forms hydrogen bond(s)). *F*, a heat map based on a proximity matrix shows that the 214-258 region of *Tg*REMIND (the extremity of the F-BAR domain) is closely associated with different residues of the REMIND domain. The average distance between two residues was calculated based on conformations observed in one 250-ns MD trajectory. Values higher than 2 nm are not shown. *G*, the average number of H-bonds *per* configuration between two given residues belonging to the BAR domain and the REMIND domain was calculated from three independent 250-ns MD trajectories (*green bars*). The values obtained independently from each trajectory are also shown (*black dots*). BAR, Bin/Amphiphysin/Rvs; DOPC, 1,2-dioleoyl-*sn*-glycero-3-phosphocholine; MD, molecular dynamics; REMIND, regulator of membrane-interacting domain.

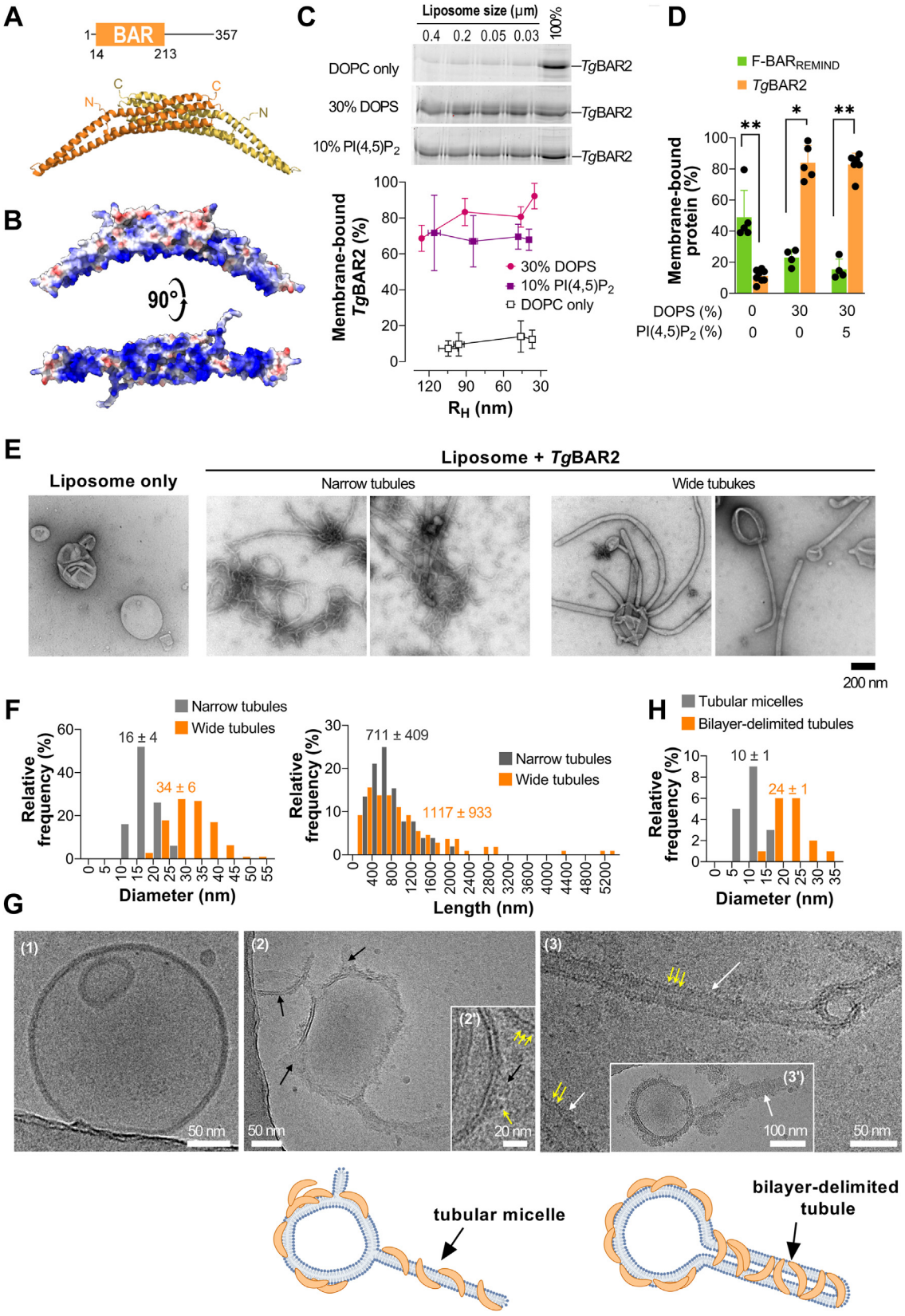

Figure 6. Membrane-binding properties of a second *T. gondii* BAR domain-containing protein. *A*, structural organization of *Tg*BAR2 and AlphaFold-predicted model of its BAR domain in a dimeric form. Its intrinsic curvature seems adapted to the recognition of 22 nm diameter tubules. The position of the N- and C-terminal ends of each monomer is shown. The structure is represented in *ribbon* mode. *B*, electrostatic potential of the dimeric BAR domain (*red* = −16.9 kTe^{-1}, *blue* = +16.9 kTe^{-1}). *C*, flotation assays. *Tg*BAR2 (0.75 µM) was incubated with liposomes of different radii (750 µM lipids), only made of DOPC or additionally containing 30% DOPS or 10% $PI(4,5)P_2$, in TN buffer for 1 h at 25 °C under agitation. The percentage of membrane-bound *Tg*BAR2 is represented as the function of the average hydrodynamic radius (R_H) of liposomes. Data correspond to mean ± SD (n = 3). *D*, flotation assays. Membrane-

from those of many F-BAR domain-containing proteins (*e.g.*, FBP17, Pacsin/Syndapin, FER, and PSTPIP) that scarcely associate with membranes unless these contain PS and PIPs (33, 34, 41). Instead, F-BAR$_{REMIND}$ has some resemblances with the F-BAR domains of yeast proteins Hof1p, Bzz1p, and Rgd1p (26), which all can significantly associate with PC membranes but not necessarily more with membranes enriched with PS or PI(4,5)P_2, except Rgd1p. Along with this, we found that introducing anionic residues in place of several basic residues, which compose a noticeable cluster in the concave membrane-binding interface of F-BAR$_{REMIND}$, only slightly decreases the avidity of this domain for PI(4,5)P_2-rich membranes. Introducing anionic residues in a hydrophobic region close to the basic cluster has much more impact. However, puzzlingly, F-BAR$_{REMIND}$ and its mutated forms can deform liposomes made of Folch fraction I lipids, *i.e.*, a mixture containing a high proportion of PS. Likely, the high protein level relative to liposome surface in tubulation assays overcomes the low affinity of F-BAR$_{REMIND}$ for negatively charged membranes and promotes binding and bending processes. We conclude that the F-BAR$_{REMIND}$ domain likely binds to membranes *via* hydrophobic interactions but also short-range interactions (potentially, electrostatic and cation-π interactions between the phosphatidylcholine headgroup and respectively positively charged residues (42) and tyrosine (43, 44)), rather than long-range electrostatic interactions.

*Tg*REMIND is promiscuously located at many internal compartments [ELC, *trans*-Golgi, dense granules, and rhoptries (20)]. We have some clues that the membrane of rhoptries is very rich in PC and sphingomyelin (45) but poor in phosphatidylinositol (PI) and PS. On the other hand, a recent study has suggested that the Golgi/*trans*-Golgi compartments, but not necessarily dense granules and rhoptries, contain a PI(4)P pool (46). However, despite these differences, *Tg*REMIND is localized on all these subcellular compartments, suggesting a capacity to target these compartments *via* nonspecific interaction in a PIP-independent manner. In agreement with this, we observed that F-BAR$_{REMIND}$, when expressed in RPE-1 cells, is primarily found at the *cis*-Golgi, which is known to be poor in negatively charged lipids and devoid of PIPs. Finally, Wan *et al.* also observed that *Tg*REMIND (called BAR1) is localized on internal compartments in *T. gondii* but is neither present at the PM nor colocalized with GAP45, a marker of the middle side IMC (facing the PM) (19). Knowing that the cytosolic leaflet of the middle side IMC and the PM is rich in PS (47), this observation fits well with our findings that the F-BAR$_{REMIND}$ barely associates with PS-rich membranes *in vitro*. Moreover, *Tg*REMIND is not localized at the PM where PI(4,5)P_2 is prominent (46), suggesting that this lipid is not a targeting determinant for that protein. Collectively, given that the REMIND domain has no membrane-binding capacity (see discussion below), we suggest that the F-BAR domain of *Tg*REMIND, as it can bind neutral membranes with low specificity and no strict requirement for PIPs, allowed this protein to be ubiquitously localized on various organelles in *T. gondii*.

In addition to characterizing the membrane-binding properties of F-BAR$_{REMIND}$, our study provides some insights into the potential function of *Tg*REMIND. We observed that F-BAR$_{REMIND}$ tends to oligomerize in solution. However, we did not observe any ability of this domain to form organized structures on tubules, *i.e.*, coat as other F-BAR domain containing proteins (30, 32). This suggests that its potential role is not to stabilize tubular structures. Moreover, we observed by negative staining that F-BAR$_{REMIND}$ only induced the formation of one, sometimes two, tubules *per* liposome, and we failed to observe tubules by cryo-EM. Two factors might explain this. First, much fewer liposomes could be detected during cryo-EM than negative-staining EM sessions; given that not all liposomes are deformed by F-BAR$_{REMIND}$, the probability of seeing tubulated liposomes by cryo-EM was possibly too low. Second, cryo-EM experiments required higher liposome and protein concentrations; we suspect that F-BAR$_{REMIND}$ at a higher concentration tends to aggregate more and that fewer copies of the protein can collectively interact with and tubulate membranes. However, by cryo-EM, we observed that F-BAR$_{REMIND}$ could bind to and disorganize the bilayer structure of liposomes. We also noted that, when overexpressed in RPE-1 cells, F-BAR$_{REMIND}$ did not induce observable membrane tubulation as found for many other BAR and F-BAR domains (34, 35) but disrupted the Golgi apparatus. Therefore, F-BAR$_{REMIND}$ has a dual ability to deform and disrupt membranes. Such a capacity to break membranes could explain why expressing this domain alone is highly toxic for *T. gondii* (20). These data suggest that *Tg*REMIND has the intrinsic ability to deform and/or disrupt endomembranes.

Next, we fully establish the existence of a new structural domain called REMIND, which was predicted to be in the second half of *Tg*REMIND, connected to the F-BAR domain *via* a disordered linker (20). Key evidence is that the C-terminal region of *Tg*REMIND has a secondary structure content

bound fraction of *Tg*BAR2 or F-BAR$_{REMIND}$ (0.75 μM) incubated with liposomes extruded through 0.1 μm pores (750 μM lipids), only made of DOPC or additionally containing 30% DOPS and 5% PI(4,5)P_2. Data correspond to mean ± SD (n = 4–8). Unpaired Mann-Whitney U test; *$p < 0.05$, **$p < 0.01$. *E*, negative-staining EM. Liposomes made of Folch fraction I lipids (30 μM) and extruded through 0.4 μm pores were incubated with *Tg*BAR2 (1.9 μM). Control experiments were conducted with liposomes only. Representative pictures are shown. *F*, diameter and length distributions of narrow and wide membrane tubules induced by *Tg*BAR2 (narrow tubules, n = 50; wide tubules, n = 112, from three independent experiments). The indicated values correspond to mean ± SD. *G*, Cryo-EM. Liposomes made of Folch fraction I lipids (150 μM lipids) and extruded through 0.4 μm pores were mixed with *Tg*BAR2 (5 μM) at P/L = 1/30 and dialyzed three times under agitation in TN buffer for 30 min at cold temperature. A control picture of liposomes without *Tg*BAR2 is shown (1). *Tg*BAR2 can transform liposomes into tubular micelles (pictures 2 and 2′ *black arrow*) and tubules delimited by a bilayer (pictures 3 and 3′, *white arrow*). *Tg*BAR2 coats the membrane surfaces and can form transmembrane densities (*yellow arrows*). Schemes are general interpretations of membrane destabilization phenomena by *Tg*BAR2; left: tubular micelles; right: bilayer-delimited tubules. *H*, diameter distribution of membrane tubules with average values observed by cryo-EM. The indicated value corresponds to mean ± SD (tubular micelles, n = 16; bilayer-delimited tubules, n = 17). BAR, Bin/Amphiphysin/Rvs; DOPC, 1,2-dioleoyl-*sn*-glycero-3-phosphocholine; DOPS, 1,2-dioleoyl-*sn*-glycero-3-phospho-L-serine; P/L, protein-to-lipid; REMIND, regulator of membrane-interacting domain.

compatible with the tridimensional model of the REMIND domain predicted by AlphaFold. Next, we show that the REMIND domain has no membrane-binding capacities, ruling out previous claims based on crude protein-lipid overlay assays and not authentic lipid bilayers (20). Most remarkably, we found that this domain, added *in trans*, prevents F-BAR$_{REMIND}$ from binding to and remodeling membranes. This means that an intramolecular association between F-BAR$_{REMIND}$ and REMIND domains might be the basis of an autoregulatory mechanism able to tune the association of *Tg*REMIND with membranes. Therefore, the REMIND domain would play a role analogous to that of the SH3 domain, which, inside Syndapin 1/Pacsin 1 (48), *Drosophila* Nervous Wreck (Nwk) (49, 50) or endophilin (51, 52) interact with the F-BAR domain (or N-BAR domain in the case of endophilin) to limit the association of these proteins with membranes. Our model is in line with several observations: the full-length *Tg*REMIND poorly binds membrane *in vitro* and does not associate with the Golgi membrane as clearly as does the F-BAR$_{REMIND}$ domain alone when expressed in RPE-1 cells. Also, as mentioned before, the transgenic expression of F-BAR$_{REMIND}$ is toxic for *T. gondii*, which indirectly suggests that the membrane-binding capacity of this domain is tightly controlled when associated with the REMIND domain (20). Moreover, structural predictions combined with MD simulations suggest that REMIND stably interacts with the tip of the F-BAR$_{REMIND}$ *via* evolutionarily conserved residues. Our data suggest that *Tg*REMIND is a membrane-disrupting device regulated by the REMIND domain. Given that this protein potentially interacts with many trafficking factors (20), we posit that one or more protein partners unlock the autoinhibition state of *Tg*REMIND and trigger its membrane remodeling capacity at different stages of the trafficking pathways. This might explain why the absence of *Tg*REMIND impacts the biogenesis of dense granules and rhoptries (20). Further work is necessary to explore this possibility.

Next, we report that *T. gondii* expresses a second BAR domain-containing protein, *Tg*BAR2, with features that highly contrast with those of the BAR domain of *Tg*REMIND. Its BAR domain is highly basic and strongly binds membranes, but only if those are enriched with negatively charged lipids. *Tg*BAR2 binds to these membranes in a rather curvature-independent manner and powerfully deforms liposomes into tubules that can be extremely narrow (~10 nm in diameter). These features are similar to those of many other BAR and N-BAR domain-containing proteins (24, 39, 53), suggesting that the function of *Tg*BAR2 would be to form and stabilize highly curved membrane structures. We additionally observed using cryo-EM that the narrow tubules formed by *Tg*BAR2 correspond to tubular micelles deriving from the outer leaflet of liposomes. Such a capacity to form tubular micelles has been identified for the N-BAR domain of endophilin-A1 (54). We noted that the concave face of the BAR domain of *Tg*BAR2 is far more basic than that of these archetypical examples of the BAR domain. These features might explain the capacity of *Tg*BAR2 to powerfully deform membranes despite its lack of AH. Therefore, the BAR domain of *Tg*BAR2 represents a new kind of BAR domain. How this is related to the function of that protein in *T. gondii* remains challenging to say. *Tg*BAR2 (under the name BAR2) has been recently reported to be, contrary to *Tg*REMIND, at the periphery of the cell, partially colocalizing with the IMC. As mentioned before, the cytosolic leaflet of the middle side IMC is particularly well-enriched in PS, and the cytosolic leaflet of PM contains both PS and PI(4,5)P_2 (46, 47). Thus, these observations fit well with our observations that *Tg*BAR2 associates *in vitro* with membranes containing both lipids. However, puzzlingly, despite its localization and ability to remodel negatively charged membranes, *Tg*BAR2 is not found at the level of the micropore, an endocytic structure derived from the parasite PM bearing dynamin-like protein *Tg*DrpC, *Tg*AP2 adaptor, and Kelch13 (21). However, it should be noted that other endocytic structures have been observed (55, 56) but have yet to be characterized from a molecular point of view. The finding that *Tg*BAR2 has a strong capability to remodel anionic membranes and, notably, to form tubular micelles that mimic the hemi-fusion stage of the neck of endocytic vesicles just before scission (54, 57) should motivate further investigations.

Experimental procedures

Plasmids

The [70–347] region of *Tg*REMIND (F-BAR$_{REMIND}$) was fused to an N-terminal His-tag and cloned into a pET-M13 plasmid (from S. Tomavo and S. Zinn-Justin, I2BC, France). Five cysteines were replaced by alanine or serine residues (C91S, C160A, C218A, C251A, and C296S mutations) to prevent protein aggregation during purification. Additional mutations in this construct were generated using the QuikChange Lightning Site-Directed Mutagenesis Kit (Agilent Technologies). The sequence of the full-length *Tg*REMIND or the [495–840] region of the protein (REMIND region) was cloned in a pGEX-6P-3 plasmid to be expressed in fusion with an N-terminal GST tag (from S. Tomavo and S. Zinn-Justin). The tag and each protein of interest are linked by a sequence (LEVLFQGPLGSGGTGQQMGRDLENLYFQG) containing a Protease PreScission cleavage site. A codon-optimized synthetic *Tg*BAR2 gene was cloned in pET-15b plasmid (ProteoGenix) to express the protein with an N-terminal His-tag. The sequence of the N-BAR domain of human amphiphysin (residues 2–242, N-BAR$_{Amph}$) was cloned into a pGEX-4T-2 plasmid to be expressed in fusion to an N-terminal GST tag (gift from Dr J.C. Stachowiak, University of Texas).

For cell biology experiments, a codon-optimized synthetic *Tg*REMIND gene was cloned in a pEGFP-C1 expression vector to express the protein in fusion with an N-terminal GFP (ProteoGenix). A stop codon was inserted in the coding sequence of *Tg*REMIND to express the [1–382] region of *Tg*REMIND appended with an N-terminal GFP (GFP-F-BAR$_{REMIND}$). Another expression vector, coding for the region [500–842] of *Tg*REMIND in fusion with GFP, was also

prepared (GFP-REMIND). The sequences of all these constructs and mutants were checked by DNA sequencing.

Protein expression and purification

All *T. gondii* proteins were expressed in *E. Coli* (BL21-GOLD(DE3)) competent cells (Stratagene) grown in Luria Bertani Broth (LB) medium at 37 °C until the optical density (A_{600}) of the bacterial suspension reached a value of 0.4 and then incubated at 18 °C until A_{600} reached 0.8. The expression of F-BAR_{REMIND} and its mutated form was induced with 0.1 mM IPTG and conducted overnight at 18 °C under agitation at 200 rpm. For *Tg*BAR2, the production occurred in similar conditions, except that the expression of the protein was induced by 0.2 mM IPTG. The bacterial cells were harvested and resuspended in cold buffer A (50 mM Tris, pH 8, 150 mM NaCl, 10 mM imidazole, and 5% (v/v) glycerol) supplemented with 1 mM PMSF, 10 μM bestatin, 1 μM pepstatin A and cOmplete, EDTA-free protease inhibitor tablets (Roche). Cells were lysed using a Cell Disruptor TS SERIES (Constant Systems Ltd), and the lysate was centrifuged at 186,000*g* for 90 min. Then, the supernatant was applied to HisPur Cobalt Resin (Thermo Fisher Scientific) for 3 h 30. The beads were washed twice with buffer A, then twice with high salt buffer (50 mM Tris, pH 8, 800 mM NaCl, 10 mM imidazole, 5% (v/v) glycerol), and twice again with buffer A. Next, the beads were incubated with 1.5 ml buffer A supplemented with 300 mM imidazole for 10 min to eluate the protein, and this step was repeated four times. The collected fractions were pooled and concentrated in an Amicon filter unit (Millipore) and further purified by size-exclusion chromatography using an XK-16/70 column packed with Sephacryl S-200 HR pre-equilibrated with buffer B (50 mM Tris, pH 8, 150 mM NaCl, 5% (v/v) glycerol). The pure protein fractions were pooled, concentrated, and supplemented with 5% (v/v) glycerol. For all these proteins, aliquots were prepared, flash-frozen in liquid nitrogen, and stored at −80 °C. The concentration of the proteins was determined by measuring their absorbency at λ = 280 nm or on SDS-PAGE compared to a range of bovine serum albumin (BSA) concentrations.

Similar purification procedures were applied for *Tg*REMIND or the REMIND construct except that buffer C (50 mM Tris, pH 8, 150 mM NaCl, 5 mM DTT, and 5% (v/v) glycerol) supplemented with 1 mM PMSF, 10 μM bestatin, 1 μM pepstatin A and cOmplete, EDTA-free protease inhibitor tablets was used to lyse the bacterial cells. Once separated from cell membranes by centrifugation, the supernatant was applied to Glutathione Sepharose 4B (Cytiva) beads for 3 h 30. The beads were washed twice with buffer C, followed by two washing steps with high salt buffer (50 mM Tris, pH 8, 800 mM NaCl, 5 mM DTT, and 5% (v/v) glycerol), and then washed twice with buffer C. Proteins were cleaved off the GST bound to resin in the presence of PreScission protease (Cytiva) in a 2 ml-volume tube overnight at 4 °C with rocking. The protein was recovered in the supernatant collected by washing the beads several times with 0.7 ml of buffer C and subjected to mild centrifugation. The protein was concentrated using an Amicon filter unit (Millipore) and purified by SEC using a Superose 6 Increase 10/300 GL column equilibrated with buffer C (supplemented with 1 mM EDTA when purifying *Tg*REMIND). The pure protein fractions were pooled, concentrated, and supplemented with 5% (v/v) glycerol to reach 10% glycerol. Each protein was stored as described before, and its concentration was determined by spectrometry or SDS-PAGE analysis.

Amphiphysin N-BAR was expressed according to the protocol reported in (58). Once the A_{600} of the bacterial suspension reached a value of 0.8, the expression of the protein was induced with 1 mM IPTG for 2 h at 37 °C under agitation of 200 rpm. Bacterial cells were harvested and resuspended with buffer C supplemented with 1 mM PMSF, 10 μM bestatin, 1 μM pepstatin A, and cOmplete, EDTA-free protease inhibitor tablets (Roche). Cells were lysed as indicated above, and the supernatant was applied to Glutathione Sepharose 4B beads. The beads were washed four times with buffer C, two times with highly salted buffer (50 mM Tris, pH 8, 800 mM NaCl, and 2 mM DTT, glycerol 5% (v/v)), and then again four times with buffer C. The protein was cleaved from the GST tag by incubating the beads with human thrombin (Sigma-Aldrich) in the presence of 50 μM $CaCl_2$ overnight at 4 °C with rocking. The protein was recovered in the supernatant after four cycles of centrifugation and washing the beads with 0.7 ml of buffer C supplemented with 2 mM EDTA. The protein was concentrated using an Amicon filter unit (Millipore) down to 1 ml. The protein was then supplemented with 5% (v/v) pure glycerol, aliquoted, flash-frozen in liquid nitrogen, and stored at −80 °C. The concentration of the proteins was determined using a BSA assay.

Lipids

18:1/18:1-PC (1,2-dioleoyl-*sn*-glycero-3-phosphocholine or DOPC), 18:1/18:1-PS (1,2-dioleoyl-*sn*-glycero-3-phospho-L-serine or DOPS), brain PI(4)P (L-α-phosphatidylinositol 4-phosphate), brain $PI(4,5)P_2$ (L-α-phosphatidylinositol 4,5-bisphosphate), and NBD-PC (1-palmitoyl-2-(12-[(7-nitro-2-1,3-benzoxadiazol-4-yl)amino]dodecanoyl)-sn-glycero-3-phosphocholine) were purchased from Avanti Polar Lipids. Lipids from bovine brain extract (Folch fraction I) and 16:0/16:0-PI(3)P were purchased from Sigma-Aldrich and Echelon Biosciences, respectively.

Liposomes preparation

Lipids stored in $CHCl_3$ or $CHCl_3$/methanol stock solutions were mixed at the desired molar ratio. The solvent was removed in a rotary evaporator under vacuum. If the flask contained a mixture with PIPs, it was prewarmed at 33 °C for 10 min before creating a vacuum. The lipid film was hydrated in 50 mM Tris, pH 7.4, 150 mM NaCl (TN) buffer to obtain a suspension of multilamellar vesicles. This suspension was frozen and thawed five times and then extruded sequentially through polycarbonate filters with pore sizes of 0.4, 0.2, 0.1, 0.05, and 0.03 μm. The liposome hydrodynamic radius (R_H) was estimated by dynamic light scattering using a Dyna Pro

instrument. Liposomes were stored at room temperature and in the dark when containing fluorescent lipids and used within 2 days.

Flotation assay

Flotation assays using liposomes of different radii were performed as described in (22). Protein association to the membrane was measured by incubating the protein (0.75 μM) with NBD-PC- containing liposomes (750 μM lipids) for 1 h at 25 °C. Then, the suspension was adjusted to 28% (w/w) sucrose by mixing 100 μl of a 60% (w/w) sucrose solution in TN buffer and overlaid with 200 μl of TN buffer containing 24% (w/w) sucrose and 50 μl of sucrose-free TN buffer. The sample was centrifuged at 240,000*g* in a swing rotor (TLS 55 Beckmann) for 70 min. The bottom (250 μl), middle (140 μl), and top (110 μl) fractions were collected. The bottom and top fractions were analyzed by SDS-PAGE after staining with SYPRO Orange using a FUSION FX fluorescence imaging system.

Electron microscopy

Liposomes (30 μM total lipids) extruded through 0.4 μm pores were mixed with protein (1.9 μM for condition P/L = 1/15) in TN buffer for 2 h. For negative staining imaging, one drop of ∼10 μl was placed on the top of a copper EM grid covered with a formvar film for 5 min and then dried and stained with uranyl acetate (1% in distilled water). The grid was examined using a JEOL JEM 1400 transmission EM at 100 kV equipped with a MORADA CCD 11 MPixels camera (Olympus SIS). For cryo-EM, 4 μl of the sample were deposited onto glow-discharged Quantifoil R2/2 holey carbon grids, blotted for 4 s with filter paper, and plunged into liquid ethane using a Vitrobot Mark IV (Thermo Fisher Scientific) operated at room temperature and 100% relative humidity. The cryo specimens were transferred into a Gatan 626 cryo-holder and observed in a JEOL 2010F electron microscope operated at 200 kV. Images were recorded at a nominal defocus of 2 μm on a Gatan K2 Summit camera under low electron-dose conditions. Images were denoised by wavelet filtration in ImageJ (https://imagej.net/ij/) using the plugin "A trous filter," $k_1 = 20$, $k_{n>1} = 0$.

Circular dichroism

The experiments were performed on a Jasco J-815 spectrometer at room temperature with a quartz cell of 0.05 cm path length. Proteins were dialyzed three times against 20 mM Tris, pH 7.4, 120 mM NaF buffer for 30 min to remove glycerol and DTT contained in protein stocks and to exchange buffer. Each spectrum is the average of 10 scans recorded from λ = 190 to 260 nm with a bandwidth of 1 nm, a step size of 0.5 nm, and a scan speed of 50 nm.min^{-1}. Protein concentration was determined at λ = 280 nm by spectrometry or by densitometry in SDS-PAGE against a BSA concentration range. A control spectrum of buffer was subtracted from each protein spectrum. The percentages of protein secondary structure were estimated by analyzing their CD spectrum (in the 190–250 nm range) using the BeStSel method provided online (59) and compared to the percentages derived from the analysis of AlphaFold-predicted structural model and conformations adopted by this model during MD simulations.

Analytical gel filtration

The various constructs were analyzed by gel filtration on a Superose 6 Increase 10/300 GL column equilibrated in TN buffer (50 mM Tris, pH 7.4, 150 mM NaCl). Calibration was performed using the following standards: apoferritin (molecular weight 443 kDa, Stokes radius 6.1 nm), alcohol dehydrogenase (150 kDa, 4.5 nm), BSA (67 kDa, 3.6 nm), carbonic anhydrase (31 kDa, 2.4 nm) and cytochrome c (12.6 kDa, 1.6 nm).

Tryptophan-fluorescence assay

Emission fluorescence spectra of protein (1 μM) in TN buffer were measured at 30 °C from 300 to 450 nm (excitation at λ_{ex} = 280 nm) in a quartz cell. The fluorescence of L-tryptophan (zwitterionic form) was recorded as a comparison.

Structural analysis

The electrostatic surfaces of proteins were calculated using ChimeraX software (https://www.cgl.ucsf.edu/chimerax/) (60) with the Coulombic electrostatic potential (ESP).

Sequence analysis

To analyze the evolutionary conservation of amino acid positions in *Tg*REMIND, protein sequences were downloaded from UniProt (https://www.uniprot.org) and analyzed with BLAST (Basic Local Alignment Search Tool) at NCBI (National Center for Biotechnology Information) using a nonredundant protein sequence database from which proteins from *T. gondii* were excluded. Alignments were analyzed with UGENE (http://ugene.net/) (61). The phylogenetic tree was visualized using the ITOL website (62). Based on the generated multiple sequence alignment, the ConSurf server was used to analyze the evolutionary conservation of amino acid positions (63–65), and the results were displayed on the three-dimensional model of *Tg*REMIND using ChimeraX software. Heliquest web server (66) was used to calculate the mean hydrophobicity, mean hydrophobic moment, and net charge along the sequence of *Tg*REMIND and *Tg*BAR2 using an 18-aa overlapping window.

MD simulation

The tridimensional structure of *Tg*REMIND (segment 72–836) has been predicted using AlphaFold (20, 67). Only the structure of the 500 to 836 region was used for the MD simulation of the REMIND domain. In all cases, the system was built with the protein or domain immersed in a water box using the TIP3P water model and was minimized and equilibrated with 120 mM NaCl using GROMACS 2021.4 MD simulation engine (https://manual.gromacs.org/2021.4/

download.html) (68) using the CHARMM36m force field (69) following the Charmm-Gui procedure (70). MD simulations were performed with GROMACS 2021.4. Bonds involving hydrogen atoms were constrained using the LINCS algorithm (71), and the integration time step was set to 2 fs. The V-rescale thermostat (72) was used to keep a temperature at 310 °K with a coupling time constant of 1 ps. For simulations with constant pressure, the Parrinello-Rahman barostat (73) was used to maintain a pressure of 1 bar with a compressibility of 4.5×10^{-5} and a coupling time constant of 2 ps. van der Waals interactions were switched to zero over 10 to 12 Å, and electrostatic interactions were evaluated using the particle mesh Ewald method (74). For *Tg*REMIND, three different MD simulations of 250 ns-length were launched using different initial seed velocities. For the REMIND domain, a 1 µs-length simulation was launched.

Analysis of MD simulations

RMSD, RMSF, H-bond analysis, and distance measurements between residues (considering mass center) were carried out using GROMACS 2021.4 (68). Home-made scripts based on Python were used to build the distance matrix. All molecular pictures and movies were made with PyMOL (https://www.pymol.org) and Visual Molecular Dynamics (www.ks.uiuc.edu/Research/vmd) (75). CD spectra were predicted from MD-generated REMIND structures using PDBMD2CD (76).

Cell culture and transfection

hRPE-1 cells (hTERT-immortalized retinal pigment epithelial cells) were obtained at ATCC (CRL-4000). Cells were maintained and grown in Dulbecco's modified Eagle medium DMEM/F12 (Gibco) supplemented with 10% fetal calf serum and 1% antibiotics (ZellShield) at 37 °C under 5% CO_2. Following the initial growth phase, the cells were seeded at a density of 40,000 cells *per* condition in an 8-well coverslip (ibidi 80826) and allowed to grow for 24 h. Subsequently, the cells were transiently transfected with 250 ng of plasmid DNA using the Lipofectamine 3000 transfection reagent (Thermo Fisher Scientific), following the manufacturer's protocol.

Immunolabeling, fluorescence microscopy, and image analysis

At different times after transfection, the cells were fixed with paraformaldehyde 4% in PBS (Thermo Fisher Scientific) for 15 min. Next, the cells were treated for 30 min with PBS supplemented with BSA 0.2% (v/v) and saponin 0.05% (v/v) at room temperature. The cells were then incubated for 1 h with primary antibodies directed against the *cis*-Golgi marker GM130 (mouse anti-GM130, BD bioscience, 610822) and/or *trans*-Golgi marker TGN46 (sheep anti-TGN46, Bio-Rad, AHP500G). Then, the cells were washed three times with PBS supplemented with BSA and saponin and incubated for 1 h with secondary fluorescent antibodies, a goat anti-mouse antibody Alexa Fluor 640, and/or a donkey anti-sheep Alexa Fluor 594 (Invitrogen). Cells were rinsed with PBS and then observed at room temperature using a Leica TCS SP8 STED 3X in confocal mode. Images were acquired through a 63 × / 1.4 NA oil objective using the LAS X software (https://www.leica-microsystems.com/products/microscope-software/p/leica-las-x-ls/, Leica Microsystems) and analyzed using ImageJ software.

Electron microscopy of cells

RPE-1 cells transfected with GFP-F-BAR_{REMIND} were fixed with 4% paraformaldehyde and 0.1% glutaraldehyde in 0.1 M phosphate, pH 7.4 buffer for 2 h. They were processed for ultracryo-microtomy using a slightly modified Tokuyasu method (77). The cell suspension was spun down in 10% gelatin. After that, the cells were immersed in 2.3 M sucrose in 0.1 M phosphate, pH 7.4 buffer overnight at 4 °C, and then rapidly frozen in liquid nitrogen. Ultrathin (70 nm thick) cryosections were prepared using an ultracryo microtome (Leica EMFCS) and mounted on formvar-coated nickel grids (Electron Microscopy Sciences). The grids were incubated successively in PBS containing the relevant primary antibody for 1 h and then incubated with PBS containing 15 nm colloidal gold-conjugated protein AG (CMC, University Medical Center, Utrecht, The Netherlands). Finally, the samples were fixed for 10 min with 1% glutaraldehyde, contrasted with a mixture of methylcellulose/sucrose and 0.3% uranyl acetate on ice. After being dried in air, sections were examined under a JEOL 1400 transmission electron microscope. The gold particles appear as dark spots, indicating the location of the GFP-F-BAR_{REMIND} within the RPE-1 cells.

Statistical analyses

Statistical analyses were performed using Prism (GraphPad). p values < 0.05, and < 0.01 are identified with 1, and 2 asterisks, respectively. The number of replicates (n) used for calculating statistics is specified in the figure legends.

Data availability

All data used in this study have been presented in the manuscript and supporting information.

Supporting information—This article contains supporting information.

Acknowledgments—We thank Dr J.C. Stachowiak and Drs. S. Zinn and S. Tomavo for plasmids and initial purification protocols. NA and this work were supported by an ANR-19-CE44-0006 grant from the Agence Nationale de la Recherche. The authors acknowledge the EM facility CCMA (Centre Commun de Microscopie Appliquée) from the « Université Côte d'Azur », part of the « Microscopie Imagerie Côte d'Azur » GIS IBiSA labeled platform, supported by Université Côte d'Azur, the "Région Sud » and the Département 06. The authors also acknowledge financial support from the CNRS-CEA network for transmission EM and atom probe studies (METSA, FR CNRS 3507) on the LPS cryo-EM platform. This work was supported by State aid under France 2030 (PhOM -Graduate School Physique) with reference ANR-11-IDEX-0003.

Author contributions—N. A.-Q., M. M., S. P., A. L., J. D., A. A. A., S. L. G., and R. G., investigation; N. A.-Q., M. M., A. L., S. L.-G., R. G. and G. D. writing–review and editing; N. A.-Q., M. M., A. L., R. G., and G. D. validation; N. A.-Q., M. M., A. L., R. G., and G. D. formal analysis; N. A.-Q., M. M., A. L., and G. D. visualization; G. D. writing–original draft; G. D. supervision; G. D. project administration; G. D. funding acquisition; G. D. conceptualization.

Conflict of interest—The authors declare that they have no conflicts of interest with the contents of this article.

Abbreviations—The abbreviations used are: AH, amphipathic helix; BAR, Bin/Amphiphysin/Rvs; BSA, bovine serum albumin; DOPC, 1,2-dioleoyl-*sn*-glycero-3-phosphocholine; DOPS, 1,2-dioleoyl-*sn*-glycero-3-phospho-L-serine; ELC, endosomal-like compartment; MIC, micronemal proteins; IMC, inner membrane complex; MD, molecular dynamics; PIPs, phosphoinositides; P/L, protein-to-lipid; PM, plasma membrane; SEC, size exclusion chromatography; REMIND, regulator of membrane-interacting domain; RMSF, root mean square fluctuation; ROP, rhoptry; RPE-1, retinal pigment epithelial-1.

References

1. Venugopal, K., and Marion, S. (2018) Secretory organelle trafficking in Toxoplasma gondii: a long story for a short travel. *Int. J. Med. Microbiol.* **308**, 751–760
2. Dogga, S. K., Mukherjee, B., Jacot, D., Kockmann, T., Molino, L., Hammoudi, P. M., *et al.* (2017) A druggable secretory protein maturase of Toxoplasma essential for invasion and egress. *eLife* **6**, e27480
3. Parussini, F., Coppens, I., Shah, P. P., Diamond, S. L., and Carruthers, V. B. (2010) Cathepsin L occupies a vacuolar compartment and is a protein maturase within the endo/exocytic system of Toxoplasma gondii. *Mol. Microbiol.* **76**, 1340–1357
4. Stasic, A. J., Moreno, S. N. J., Carruthers, V. B., and Dou, Z. (2022) The Toxoplasma plant-like vacuolar compartment (PLVAC). *J. Eukaryot. Microbiol.* **69**, e12951
5. Griffith, M. B., Pearce, C. S., and Heaslip, A. T. (2022) Dense granule biogenesis, secretion, and function in Toxoplasma gondii. *J. Eukaryot. Microbiol.* **69**, e12904
6. Kremer, K., Kamin, D., Rittweger, E., Wilkes, J., Flammer, H., Mahler, S., *et al.* (2013) An overexpression screen of Toxoplasma gondii Rab-GTPases reveals distinct transport routes to the micronemes. *PLoS Pathog.* **9**, e1003213
7. Tomavo, S., Slomianny, C., Meissner, M., and Carruthers, V. B. (2013) Protein trafficking through the endosomal system prepares intracellular parasites for a home invasion. *PLoS Pathog.* **9**, e1003629
8. Chaturvedi, S., Qi, H., Coleman, D., Rodriguez, A., Hanson, P. I., Striepen, B., *et al.* (1999) Constitutive calcium-independent release of Toxoplasma gondii dense granules occurs through the NSF/SNAP/SNARE/Rab machinery. *J. Biol. Chem.* **274**, 2424–2431
9. Jackson, A. J., Clucas, C., Mamczur, N. J., Ferguson, D. J., and Meissner, M. (2013) Toxoplasma gondii Syntaxin 6 is required for vesicular transport between endosomal-like compartments and the Golgi complex. *Traffic* **14**, 1166–1181
10. Pfluger, S. L., Goodson, H. V., Moran, J. M., Ruggiero, C. J., Ye, X., Emmons, K. M., *et al.* (2005) Receptor for retrograde transport in the apicomplexan parasite Toxoplasma gondii. *Eukaryot. Cell* **4**, 432–442
11. Ngô, H. M., Yang, M., Paprotka, K., Pypaert, M., Hoppe, H., and Joiner, K. A. (2003) AP-1 in Toxoplasma gondii mediates biogenesis of the rhoptry secretory organelle from a post-Golgi compartment. *J. Biol. Chem.* **278**, 5343–5352
12. Morlon-Guyot, J., Pastore, S., Berry, L., Lebrun, M., and Daher, W. (2015) Toxoplasma gondii Vps11, a subunit of HOPS and CORVET tethering complexes, is essential for the biogenesis of secretory organelles. *Cell Microbiol.* **17**, 1157–1178
13. Sangaré, L. O., Alayi, T. D., Westermann, B., Hovasse, A., Sindikubwabo, F., Callebaut, I., *et al.* (2016) Unconventional endosome-like compartment and retromer complex in Toxoplasma gondii govern parasite integrity and host infection. *Nat. Commun.* **7**, 11191
14. Breinich, M. S., Ferguson, D. J., Foth, B. J., van Dooren, G. G., Lebrun, M., Quon, D. V., *et al.* (2009) A dynamin is required for the biogenesis of secretory organelles in Toxoplasma gondii. *Curr. Biol.* **19**, 277–286
15. Di Cristina, M., Spaccapelo, R., Soldati, D., Bistoni, F., and Crisanti, A. (2000) Two conserved amino acid motifs mediate protein targeting to the micronemes of the apicomplexan parasite Toxoplasma gondii. *Mol. Cell Biol.* **20**, 7332–7341
16. Hoppe, H. C., Ngô, H. M., Yang, M., and Joiner, K. A. (2000) Targeting to rhoptry organelles of Toxoplasma gondii involves evolutionarily conserved mechanisms. *Nat. Cell Biol.* **2**, 449–456
17. Simunovic, M., Evergren, E., Callan-Jones, A., and Bassereau, P. (2019) Curving cells inside and out: roles of BAR domain proteins in membrane shaping and its cellular implications. *Annu. Rev. Cell Dev. Biol.* **35**, 111–129
18. McGovern, O. L., Rivera-Cuevas, Y., and Carruthers, V. B. (2021) Emerging mechanisms of endocytosis in Toxoplasma gondii. *Life (Basel)* **11**, 84
19. Wan, W., Dong, H., Lai, D.-H., Yang, J., He, K., Tang, X., *et al.* (2023) The Toxoplasma micropore mediates endocytosis for selective nutrient salvage from host cell compartments. *Nat. Commun.* **14**, 977
20. Houngue, R., Sangaré, L. O., Alayi, T. D., Dieng, A., Bitard-Feildel, T., Boulogne, C., *et al.* (2023) Toxoplasma membrane inositol phospholipid binding protein TgREMIND is essential for secretory organelle function and host infection. *Cell Rep.* **43**, 113601
21. Koreny, L., Mercado-Saavedra, B. N., Klinger, C. M., Barylyuk, K., Butterworth, S., Hirst, J., *et al.* (2023) Stable endocytic structures navigate the complex pellicle of apicomplexan parasites. *Nat. Commun.* **14**, 2167
22. Drin, G., Casella, J. F., Gautier, R., Boehmer, T., Schwartz, T. U., and Antonny, B. (2007) A general amphipathic alpha-helical motif for sensing membrane curvature. *Nat. Struct. Mol. Biol.* **14**, 138–146
23. Manneville, J. B., Leduc, C., Sorre, B., and Drin, G. (2012) Studying in vitro membrane curvature recognition by proteins and its role in vesicular trafficking. *Methods Cell Biol.* **108**, 47–71
24. Peter, B. J., Kent, H. M., Mills, I. G., Vallis, Y., Butler, P. J., Evans, P. R., *et al.* (2004) BAR domains as sensors of membrane curvature: the amphiphysin BAR structure. *Science* **303**, 495–499
25. Zeno, W. F., Snead, W. T., Thatte, A. S., and Stachowiak, J. C. (2019) Structured and intrinsically disordered domains within Amphiphysin1 work together to sense and drive membrane curvature. *Soft Matter* **15**, 8706–8717
26. Moravcevic, K., Alvarado, D., Schmitz, K. R., Kenniston, J. A., Mendrola, J. M., Ferguson, K. M., *et al.* (2015) Comparison of Saccharomyces cerevisiae F-BAR domain structures reveals a conserved inositol phosphate binding site. *Structure* **23**, 352–363
27. Shimada, A., Niwa, H., Tsujita, K., Suetsugu, S., Nitta, K., Hanawa-Suetsugu, K., *et al.* (2007) Curved EFC/F-BAR-domain dimers are joined end to end into a filament for membrane invagination in endocytosis. *Cell* **129**, 761–772
28. Wang, Q., Navarro, M. V., Peng, G., Molinelli, E., Goh, S. L., Judson, B. L., *et al.* (2009) Molecular mechanism of membrane constriction and tubulation mediated by the F-BAR protein Pacsin/Syndapin. *Proc. Natl. Acad. Sci. U. S. A.* **106**, 12700–12705
29. Tanaka-Takiguchi, Y., Itoh, T., Tsujita, K., Yamada, S., Yanagisawa, M., Fujiwara, K., *et al.* (2013) Physicochemical analysis from real-time imaging of liposome tubulation reveals the characteristics of individual F-BAR domain proteins. *Langmuir* **29**, 328–336
30. Frost, A., Perera, R., Roux, A., Spasov, K., Destaing, O., Egelman, E. H., *et al.* (2008) Structural basis of membrane invagination by F-BAR domains. *Cell* **132**, 807–817
31. McDonald, N. A., Takizawa, Y., Feoktistova, A., Xu, P., Ohi, M. D., Vander Kooi, C. W., *et al.* (2016) The tubulation activity of a fission yeast

F-BAR protein is dispensable for its function in cytokinesis. *Cell Rep.* **14**, 534–546
32. Henne, W. M., Kent, H. M., Ford, M. G., Hegde, B. G., Daumke, O., Butler, P. J., *et al.* (2007) Structure and analysis of FCHo2 F-BAR domain: a dimerizing and membrane recruitment module that effects membrane curvature. *Structure* **15**, 839–852
33. Itoh, T., Erdmann, K. S., Roux, A., Habermann, B., Werner, H., and De Camilli, P. (2005) Dynamin and the actin cytoskeleton cooperatively regulate plasma membrane invagination by BAR and F-BAR proteins. *Dev. Cel.* **9**, 791–804
34. Tsujita, K., Suetsugu, S., Sasaki, N., Furutani, M., Oikawa, T., and Takenawa, T. (2006) Coordination between the actin cytoskeleton and membrane deformation by a novel membrane tubulation domain of PCH proteins is involved in endocytosis. *J. Cell Biol.* **172**, 269–279
35. Shimada, A., Takano, K., Shirouzu, M., Hanawa-Suetsugu, K., Terada, T., Toyooka, K., *et al.* (2010) Mapping of the basic amino-acid residues responsible for tubulation and cellular protrusion by the EFC/F-BAR domain of pacsin2/Syndapin II. *FEBS Lett.* **584**, 1111–1118
36. Ramesh, P., Baroji, Y. F., Reihani, S. N., Stamou, D., Oddershede, L. B., and Bendix, P. M. (2013) FBAR syndapin 1 recognizes and stabilizes highly curved tubular membranes in a concentration dependent manner. *Sci. Rep.* **3**, 1565
37. Bai, X., Meng, G., Luo, M., and Zheng, X. (2012) Rigidity of wedge loop in PACSIN 3 protein is a key factor in dictating diameters of tubules. *J. Biol. Chem.* **287**, 22387–22396
38. Farsad, K., Ringstad, N., Takei, K., Floyd, S. R., Rose, K., and De Camilli, P. (2001) Generation of high curvature membranes mediated by direct endophilin bilayer interactions. *J. Cell Biol.* **155**, 193–200
39. Masuda, M., Takeda, S., Sone, M., Ohki, T., Mori, H., Kamioka, Y., *et al.* (2006) Endophilin BAR domain drives membrane curvature by two newly identified structure-based mechanisms. *EMBO J.* **25**, 2889–2897
40. Salzer, U., Kostan, J., and Djinović-Carugo, K. (2017) Deciphering the BAR code of membrane modulators. *Cell Mol. Life Sci.* **74**, 2413–2438
41. Dharmalingam, E., Haeckel, A., Pinyol, R., Schwintzer, L., Koch, D., Kessels, M. M., *et al.* (2009) F-BAR proteins of the syndapin family shape the plasma membrane and are crucial for neuromorphogenesis. *J. Neurosci.* **29**, 13315–13327
42. Spuhler, P., Anantharamaiah, G. M., Segrest, J. P., and Seelig, J. (1994) Binding of apolipoprotein A-I model peptides to lipid bilayers. Measurement of binding isotherms and peptide-lipid headgroup interactions. *J. Biol. Chem.* **269**, 23904–23910
43. Roberts, M. F., Gershenson, A., and Reuter, N. (2022) Phosphatidylcholine cation-tyrosine π complexes: motifs for membrane binding by a bacterial phospholipase C. *Molecules* **27**, 6184
44. Hirano, Y., Gao, Y. G., Stephenson, D. J., Vu, N. T., Malinina, L., Simanshu, D. K., *et al.* (2019) Structural basis of phosphatidylcholine recognition by the C2-domain of cytosolic phospholipase A(2)α. *eLife* **8**, e44760
45. Besteiro, S., Bertrand-Michel, J., Lebrun, M., Vial, H., and Dubremetz, J. F. (2008) Lipidomic analysis of Toxoplasma gondii tachyzoites rhoptries: further insights into the role of cholesterol. *Biochem. J.* **415**, 87–96
46. [preprint] Arabiotorre, A., Formanowicz, M., Bankaitis, V. A., and Grabon, A. (2023) Phosphatidylinositol-4-phosphate signaling regulates dense granule biogenesis and exocytosis in Toxoplasma gondii. *bioRxiv*. https://doi.org/10.1101/2023.01.09.523261
47. Konishi, R., Fukuda, K., Kuriyama, S., Masatani, T., Xuan, X., and Fujita, A. (2023) Unique asymmetric distribution of phosphatidylserine and phosphatidylethanolamine in Toxoplasma gondii revealed by nanoscale analysis. *Histochem. Cell Biol.* **160**, 279–291
48. Rao, Y., Ma, Q., Vahedi-Faridi, A., Sundborger, A., Pechstein, A., Puchkov, D., *et al.* (2010) Molecular basis for SH3 domain regulation of F-BAR-mediated membrane deformation. *Proc. Natl. Acad. Sci. U. S. A.* **107**, 8213–8218
49. Kelley, C. F., Messelaar, E. M., Eskin, T. L., Wang, S., Song, K., Vishnia, K., *et al.* (2015) Membrane charge directs the outcome of F-BAR domain lipid binding and autoregulation. *Cell Rep.* **13**, 2597–2609
50. Stanishneva-Konovalova, T. B., Kelley, C. F., Eskin, T. L., Messelaar, E. M., Wasserman, S. A., Sokolova, O. S., *et al.* (2016) Coordinated autoinhibition of F-BAR domain membrane binding and WASp activation by Nervous Wreck. *Proc. Natl. Acad. Sci. U. S. A.* **113**, E5552–E5561
51. Bhatt, V. S., Ashley, R., and Sundborger-Lunna, A. (2021) Amphipathic motifs regulate N-BAR protein endophilin B1 auto-inhibition and drive membrane remodeling. *Structure* **29**, 61–69.e63
52. Chen, Z., Chang, K., Capraro, B. R., Zhu, C., Hsu, C. J., and Baumgart, T. (2014) Intradimer/Intermolecular interactions suggest autoinhibition mechanism in endophilin A1. *J. Am. Chem. Soc.* **136**, 4557–4564
53. Gallop, J. L., Jao, C. C., Kent, H. M., Butler, P. J. G., Evans, P. R., Langen, R., *et al.* (2006) Mechanism of endophilin N-BAR domain-mediated membrane curvature. *EMBO J.* **25**, 2898–2910
54. Mizuno, N., Jao, C. C., Langen, R., and Steven, A. C. (2010) Multiple modes of endophilin-mediated conversion of lipid vesicles into coated tubes: implications for synaptic endocytosis. *J. Biol. Chem.* **285**, 23351–23358
55. Gras, S., Jimenez-Ruiz, E., Klinger, C. M., Schneider, K., Klingl, A., Lemgruber, L., *et al.* (2019) An endocytic-secretory cycle participates in Toxoplasma gondii in motility. *PLoS Biol.* **17**, e3000060
56. Nolan, S. J., Romano, J. D., and Coppens, I. (2017) Host lipid droplets: an important source of lipids salvaged by the intracellular parasite Toxoplasma gondii. *PLoS Pathog.* **13**, e1006362
57. Bashkirov, P. V., Akimov, S. A., Evseev, A. I., Schmid, S. L., Zimmerberg, J., and Frolov, V. A. (2008) GTPase cycle of dynamin is coupled to membrane squeeze and release, leading to spontaneous fission. *Cell* **135**, 1276–1286
58. Snead, W. T., Zeno, W. F., Kago, G., Perkins, R. W., Richter, J. B., Zhao, C., *et al.* (2019) BAR scaffolds drive membrane fission by crowding disordered domains. *J. Cell Biol.* **218**, 664–682
59. Micsonai, A., Wien, F., Kernya, L., Lee, Y.-H., Goto, Y., Réfrégiers, M., *et al.* (2015) Accurate secondary structure prediction and fold recognition for circular dichroism spectroscopy. *Proc. Natl. Acad. Sci. U. S. A.* **112**, E3095–E3103
60. Pettersen, E. F., Goddard, T. D., Huang, C. C., Meng, E. C., Couch, G. S., Croll, T. I., *et al.* (2021) UCSF ChimeraX: structure visualization for researchers, educators, and developers. *Protein Sci.* **30**, 70–82
61. Okonechnikov, K., Golosova, O., Fursov, M., and UGENE team (2012) Unipro UGENE: a unified bioinformatics toolkit. *Bioinformatics* **28**, 1166–1167
62. Letunic, I., and Bork, P. (2021) Interactive Tree of Life (iTOL) v5: an online tool for phylogenetic tree display and annotation. *Nucleic Acids Res.* **49**, W293–W296
63. Goldenberg, O., Erez, E., Nimrod, G., and Ben-Tal, N. (2009) The ConSurf-DB: pre-calculated evolutionary conservation profiles of protein structures. *Nucleic Acids Res.* **37**, D323–D327
64. Ben Chorin, A., Masrati, G., Kessel, A., Narunsky, A., Sprinzak, J., Lahav, S., *et al.* (2020) ConSurf-DB: an accessible repository for the evolutionary conservation patterns of the majority of PDB proteins. *Protein Sci.* **29**, 258–267
65. Yariv, B., Yariv, E., Kessel, A., Masrati, G., Chorin, A. B., Martz, E., *et al.* (2023) Using evolutionary data to make sense of macromolecules with a "face-lifted" ConSurf. *Protein Sci.* **32**, e4582
66. Gautier, R., Douguet, D., Antonny, B., and Drin, G. (2008) HELIQUEST: a web server to screen sequences with specific alpha-helical properties. *Bioinformatics* **24**, 2101–2102
67. Jumper, J., Evans, R., Pritzel, A., Green, T., Figurnov, M., Ronneberger, O., *et al.* (2021) Highly accurate protein structure prediction with AlphaFold. *Nature* **596**, 583–589
68. Abraham, M. J., Murtola, T., Schulz, R., Páll, S., Smith, J. C., Hess, B., *et al.* (2015) GROMACS: high performance molecular simulations through multi-level parallelism from laptops to supercomputers. *SoftwareX* **1-2**, 19–25
69. Huang, J., Rauscher, S., Nawrocki, G., Ran, T., Feig, M., de Groot, B. L., *et al.* (2017) CHARMM36m: an improved force field for folded and intrinsically disordered proteins. *Nat. Methods* **14**, 71–73

70. Li Manni, G., Fdez. Galván, I., Alavi, A., Aleotti, F., Aquilante, F., Autschbach, J., *et al*. (2023) The OpenMolcas web: a community-driven approach to advancing computational chemistry. *J. Chem. Theor. Comput.* **19**, 6933–6991
71. Hess, B. (2008) P-LINCS: a parallel linear constraint solver for molecular simulation. *J. Chem. Theor. Comput.* **4**, 116–122
72. Bussi, G., Donadio, D., and Parrinello, M. (2007) Canonical sampling through velocity rescaling. *J. Chem. Phys.* **126**, 014101
73. Parrinello, M., and Rahman, A. (1981) Polymorphic transitions in single crystals: a new molecular dynamics method. *J. Appl. Phys.* **52**, 7182–7190
74. Essmann, U., Perera, L., Berkowitz, M. L., Darden, T., Lee, H., and Pedersen, L. G. (1995) A smooth particle mesh Ewald method. *J. Chem. Phys.* **103**, 8577–8593
75. Humphrey, W., Dalke, A., and Schulten, K. (1996) VMD: Visual molecular dynamics. *J. Mol. Graphics* **14**, 33–38
76. Drew, E. D., and Janes, R. W. (2020) PDBMD2CD: providing predicted protein circular dichroism spectra from multiple molecular dynamics-generated protein structures. *Nucleic Acids Res.* **48**, W17–W24
77. Tokuyasu, K. T. (1973) A technique for ultracryotomy of cell suspensions and tissues. *J. Cell Biol.* **57**, 551–565